

THESIS FOR THE DEGREE OF DOCTOR OF PHILOSOPHY

Quantum theory of time-dependent transport in graphene

YEVGENIY KORNIYENKO

Applied Quantum Physics Laboratory
Department of Microtechnology and Nanoscience
CHALMERS UNIVERSITY OF TECHNOLOGY
Gothenburg, Sweden 2017

Quantum theory of time-dependent transport in graphene
Yevgeniy Korniyenko

ISBN 978-91-7597-590-0

©Yevgeniy Korniyenko, 2017

Doktorsavhandlingar vid Chalmers tekniska högskola
Ny serie nr 4271
ISSN 0346-718X

Applied Quantum Physics Laboratory
Department of Microtechnology and Nanoscience - MC2
Chalmers University of Technology
SE-412 96 Göteborg, Sweden
Telephone +46 (0)31-772 1000
www.chalmers.se

Author email: yevgeniy@chalmers.se

ISSN 1652-0769
Technical Report MC2-365

Printed by Chalmers Reproservice
Göteborg, Sweden 2017

Quantum theory of time-dependent transport in graphene
YEVGENIY KORNIYENKO

Applied Quantum Physics Laboratory
Department of Microtechnology and Nanoscience - MC2
Chalmers University of Technology, 2017

Abstract

High-quality ballistic electronic devices made from graphene are becoming an experimental reality. Carbon-based electronics is heralded if not to succeed or surpass then to complement the existing semiconducting technology. This thesis investigates graphene-based devices from a theoretical point of view with the focus on high-frequency applications, where the material is expected to have a large impact. We develop a quantum-mechanical description of time-dependent transport in mesoscopic graphene samples based on a scattering matrix approach similar to Landauer-Büttiker treatment of non-relativistic charge carriers. We investigate scattering processes involved in transport through a GFET and identify resonant mechanisms that lead to enhancement of the source-drain current under an oscillating gate signal. We propose a tunable selective frequency multiplication scheme and a radiation detector with operation relying on such mechanisms. The performance of the proposed devices is investigated in terms of their shot noise and Fano factor, which we show to be suppressed due to Klein tunnelling even for strong driving of the system. Finally, we apply the formalism to a quantum pump based on an asymmetric potential profile with respect to the gate electrode doping and compute the current through it, revealing that the temperature and the back gate bias can be used to switch the direction of the current.

Keywords: graphene, ballistic quantum transport, Floquet scattering matrix, Fano resonance, Landauer-Büttiker theory

List of publications

This thesis is based on the work contained in the following papers, referred to by Roman numerals in the text:

I Resonant second-harmonic generation in a ballistic graphene transistor with an ac-driven gate

Y. Korniyenko, O. Shevtsov, and T. Löfwander
Phys. Rev. B **93**, 035435 (2016)

II Nonlinear response of a ballistic graphene transistor with an ac-driven gate: High harmonic generation and terahertz detection

Y. Korniyenko, O. Shevtsov, and T. Löfwander
Phys. Rev. B **94**, 125445 (2016)

III Shot noise in a harmonically driven ballistic graphene transistor

Y. Korniyenko, O. Shevtsov, and T. Löfwander
Phys. Rev. B **95**, 165420 (2017)

IV Resonant single-parameter pumping in graphene

Y. Korniyenko, O. Shevtsov, and T. Löfwander
Submitted to Phys. Rev. B, arXiv:1705.05350v1 [cond-mat.mes-hall]

Contents

List of publications	v
Contents	vii
List of figures	xi
Nomenclature	xiii
1 Introduction	1
1.1 Graphene	1
1.2 Motivation	3
1.3 Thesis outline	3
2 Graphene essentials	5
2.1 Basic properties	5
2.1.1 Crystal structure	5
2.1.2 Dirac Hamiltonian	6
2.2 Fabrication	9
2.3 Graphene FET	12
3 Quantum tunnelling	15
3.1 Single barrier tunnelling	15
3.1.1 Non-relativistic tunnelling	16
3.1.2 Klein tunnelling	19
3.1.3 Pseudospin matching	22
3.2 Bound states	24
3.2.1 Non-relativistic wells	24
3.2.2 Relativistic wells	25
3.3 Double barrier tunnelling	25

4	AC field scattering	29
4.1	Tien-Gordon theory.	29
4.1.1	Bessel functions	31
4.2	Oscillating delta-barrier in Schrödinger equation	33
4.3	Floquet theory in graphene	36
4.3.1	Magnus expansion of the boundary condition	40
5	Transport theory	43
5.1	Electron current in second quantization	43
5.1.1	Historical perspective	43
5.1.2	Transverse modes	44
5.1.3	Scattering basis	46
5.1.4	Field operators in second quantization	47
5.1.5	Scattering matrix	49
5.1.6	Statistical averages	52
5.2	Floquet scattering matrix	54
5.2.1	Scattering formalism in graphene	56
5.2.2	Current noise	57
6	Paper overview	59
6.1	Paper I	59
6.2	Paper II	60
6.3	Paper III	61
6.4	Paper IV	62
7	Summary and outlook	63
	Acknowledgements	65
	Appendices	66
A	Graphene tight-binding Hamiltonian	67
B	Delta potential boundary condition	71
B.1	Static barrier in Schrödinger equation	71
B.2	Static barrier in Dirac equation	72
B.3	Dynamic barrier in Schrödinger equation	73

C	Bound states in a square well	77
C.1	2DEG	77
C.2	Graphene	78
D	Commutation relations	79
E	Fermi-Dirac distribution limits	81
	Bibliography	83
	Appended papers	95
	Paper I	95
	Paper II	109
	Paper III	127
	Paper IV	139

List of figures

2.1	Graphene lattice.	6
2.2	Energy bands of graphene	8
3.1	Length scales separation	16
3.2	1D rectangular and delta potential barriers	17
3.3	Rectangular and delta barrier transmission for Schrödinger equation	19
3.4	Rectangular and delta barrier transmission for Dirac equation	20
3.5	Pseudospin matching	23
3.6	Scattering from an asymmetric double barrier	26
3.7	Double barrier in graphene.	28
4.1	Bessel functions	32
4.2	Transmission through an oscillating delta barrier	34
4.3	Fano resonance energy levels	35
4.4	Fano resonances	36
4.5	Scattering from an oscillating barrier in graphene	38
4.6	Oscillation-induced Dirac cone sections	39
5.1	Conductance through QPC	45
5.2	Multi-terminal scattering	49

Nomenclature

2DEG	Two-dimensional electron gas
FET	Field-effect transistor
GFET	Graphene FET
QPC	Quantum point contact
1D	One-dimensional
2D	Two-dimensional
DC	Direct current
AC	Alternating current
SE	Schrödinger equation
Tr	Trace of a matrix
H	Hamiltonian
a_0	Lattice parameter
v_F	Fermi velocity in graphene
$\sigma_{x,y}$	Pauli matrices
h	Planck constant
\hbar	Reduced Planck constant
Ψ	Wavefunction of a charge carrier
E	Energy of a charge carrier
K, K'	Dirac points
$\phi_{A,B}$	Atomic wavefunctions
\mathbf{k}	Wavevector of a particle
\mathbf{j}	Probability current density
U_0	Static barrier height
U_1	Dynamic barrier height perturbation
D	Barrier width
t	Time
Ξ	Reservoir temperature
t_n	Tunneling amplitude to the n^{th} sideband
r_n	Reflection amplitude to the n^{th} sideband
S	Scattering matrix
ϕ_n	Angle of incidence at the n^{th} sideband
i	Imaginary unit
I	Current
G	Conductance
e	Electron charge
V_{LR}	Source-drain voltage bias

Ω	AC driving frequency
J_n	n^{th} order Bessel function of the first kind
N	Noise
f_α	Fermi distribution in reservoir α
Re	Real part
Im	Imaginary part
Int	Integer part

Chapter 1

Introduction

1.1 Graphene

Carbon is the fourth most abundant element in the universe by mass and the second after oxygen in the human body. It is a key component of living organisms as we know them. The element has been known to mankind since antiquity making it one of the most studied subjects. Yet it seems we still have many things to discover about it. The key to its abundance in organic matter lies perhaps in the fact that it has 4 valence electrons available to make bonds with other atoms. In fact, the electronic configuration of Carbon is $1s^2 2s^2 2p^2$, allowing one of the outer shell s electrons to promote itself to the p subshell when forming a bond with another atom. In addition, the Carbon atom is the smallest among group IV of the periodic table of elements, making its covalent bond to itself the strongest among those. Its ability to form long covalent bond chains is the basis of the great number of organic compounds that are present on earth. Speaking of pure Carbon compounds, 4 valence electrons allow it to be in several different bond configurations, hybridizations sp , sp^2 and sp^3 formed by hybridization of its s and p orbital electrons. One of the most well-known allotropes of Carbon, diamond has sp^3 hybridization, forcing the Carbon atoms to form tetrahedral structures, responsible for high mechanical hardness of diamond. On the other hand, it involves all of available electrons in bond formation, making diamond a great insulator. Carbon in sp^2 configuration is found in graphite. Despite it being readily available to mankind, the internal structure of graphite in commonly used pencil remained unclear until early 20th century. The crystallographic structure of it contains plains of

carbon atoms loosely held together by van der Waals forces. The relative ease with which these bonds break is responsible for success of pencil as a writing tool (until MS Word was invented, of course). A single layer of graphite, graphene has not been studied well until Wallace [1] derived its band structure in 1947. The reason for the lack of study on the material lies perhaps in the fact that it is just a single layer of atoms and precision of available technology had to catch up. The major discovery by Wallace was that graphene displayed a linear band structure close to corners of the Brillouin zone. Such a dispersion relation is typical for relativistic particles, while common materials all display a quadratic dispersion relation. Moving forward, the parallel between it and Dirac particles was drawn by the late 20th century [2]. But it was still not until 2004 [3] when the material was actually confirmed to exist on its own experimentally. Knowing that physical systems can be mapped onto each other if their Hamiltonians have the same structure, one can only imagine the excitement of the scientific community when, quoting M. I. Katsnelson, "CERN on one's desk" became available. It allowed to test exotic physical phenomena that could be observed only in high-energy physics. The extensive studies of it revealed a number of other interesting properties that might not have been foreseen by Wallace 70 years ago.

The unusual dispersion relation of graphene supports fundamental studies of exotic effects like anomalous Quantum Hall regime [4], Veselago lensing [5] and Klein tunneling [6]. Its crystal structure guarantees mechanical robustness, making it one of the strongest materials available [7]. Graphene, being just one atom thin presents a higher level of electron confinement to a single plane than even two-dimensional electron gas (2DEG). On top of that, delocalized π -bonds in sp^2 hybridization provide graphene with remarkable electronic and thermal conductivity [8, 9].

As graphene possesses a unique combination of mechanical, electrical and thermal properties, it is still attracting large interest of the scientific community. In addition, the discovery of graphene has boosted research into other possible two-dimensional materials, with obvious candidates of silicene and germanene [10, 11], but the list now includes many more, e.g. BN [12] and MoS₂ [13]. Such materials display fascinating properties of their own and/or can be complementary to graphene. An interesting direction of research is combining these planar materials into heterostructures [14, 15], producing new material properties not achievable in either of the individual components. The number of applications of the material is con-

stantly growing and the reader is kindly referred to many review papers on the subject [16–19] to learn more about intriguing properties of graphene.

1.2 Motivation

As graphene fabrication technology is leaping forward, high-quality defect-free graphene samples can be produced nowadays with electronic mean free paths over a micron long [20, 21]. On one hand, it allows to study very exotic phenomena like hydrodynamics of electrons in graphene [22, 23] which is only possible when the electron-phonon interactions are no longer the most dominant relaxation mechanism, but rather electron-electron interactions start to play a major role. On the other hand, ballistic devices in combination with high electron mobility, tunable charge density and interesting properties of graphene beg for research into high-frequency applications of it. The experimental effort in this direction has enjoyed a moderate success with graphene-based field-effect transistors (FETs), frequency multipliers, and detectors produced [24–26]. The aim of this project is to examine the possibility of utilizing graphene in high-mobility transistors for high-frequency applications from a theoretical point of view. On one side we have ballistic transport which is an interesting field of research in itself, on the other RF electronics has a so-called terahertz gap [27], meaning that there are fewer high-quality sources and detectors in this frequency range. Studying graphene as a possible candidate for bridging this gap is one target of the thesis. From a theoretical point of view, there exists a description of mesoscopic conduction in 2DEGs, the so-called Landauer-Büttiker [28] theory. However, unique properties of graphene call for reexamination of this theory and development of a quantum theory of mesoscopic time-dependent transport in the context of Dirac fermions, which is another goal of this work.

1.3 Thesis outline

In this section we provide the reader with this book’s structure. It is a compilation thesis, meaning that the main research findings of the author are presented in the form of appended papers. The main text of the thesis is aimed at giving the reader a comprehensive introduction to the concepts used in the papers, establishing the relation between them and putting the

thesis into a broader perspective. The main text and the appended papers should therefore be viewed as complementary to each other.

Chapter 2 introduces basic concepts about graphene as a material. Starting with its crystal structure, we derive its low energy electronic band structure based on a tight-binding model, followed by an overview of presently used graphene fabrication techniques with their respective fields of use. Finally, a graphene-based field-effect transistor, related to all of the appended papers, is discussed, and its possible applications in electronics are mentioned together with the current state of the field.

In Chapter 3 the core notions behind electron transport through a static potential landscape are introduced, which lays the foundation for the discussion in the chapters that follow. We describe quantum-mechanical phenomena in simple setups, introducing concepts of Fabry-Pérot interference, tunnelling through potential barriers and formation of bound states in potential wells. The boundary conditions for rectangular and delta barrier in graphene are analysed and compared to the analogous setups in materials with quadratic dispersion relation. All these concepts play an important role in the appended papers. Double barrier tunnelling is introduced to supplement discussion in Paper II.

The framework built in the preceding chapters is expanded in Chapter 4 by introducing a time-dependent potential. The solution strategies to Schrödinger and Dirac equations with such term are discussed in the context of Tien-Gordon theory. We analyse formation of sidebands and associated inelastic processes governing scattering from a harmonic scatterer. In particular, Fano and Breit-Wigner resonances are described, their formation is the main subject of study in Paper I.

We present the main theoretical tool used in all of the appended papers, namely the scattering theory, in Chapter 5. All important steps in the development of it in relation to mesoscopic transport in 2DEG are outlined, introducing waveguides, scattering matrix and its Floquet state analogue and statistical averages of operators, finally arriving at the electronic current. We conclude the chapter with remarks about the scattering theory in graphene, developed in Paper I and used in subsequent papers, which is perhaps the most important result of the research presented in this work.

A short overview of the developments in each of the appended papers is presented in Chapter 6. We proceed with summary and outlook for possible extensions and improvements of the presented work in Chapter 7, which concludes the thesis.

Chapter 2

Graphene essentials

2.1 Basic properties

In this chapter we review some of the fundamental properties of graphene, its crystal structure and how it manifests itself in a relativistic low energy dispersion relation in particular. We present an overview of common fabrication techniques and possible fields of use in graphene technology. Finally we show an idea behind graphene-based field-effect transistor devices along with the current progress and challenges in the field.

2.1.1 Crystal structure

Monolayer graphene is a two-dimensional carbon allotrope with C atoms arranged in a honeycomb lattice, as shown in Fig. 2.1 (a). The carbon-carbon bond length is $a_0 = 1.42 \text{ \AA}$. Carbon atoms are in sp^2 hybridization, with covalently bound to three neighbours, leaving exactly one p_z -orbital electron per atom. Due to the dumbbell shape of p-orbitals, these electrons form a continuous conjugated π -bond above and below the atomic plane, which is responsible for the great electrical conductivity of it. One can note that a_0 is shorter than a normal sp^2 -hybridized carbon bond of 1.47 \AA exactly due to the additional π bond.

Graphene's unit cell consists of two inequivalent atoms, or in other words there are two sublattices that are inequivalent from a crystallographic point of view, we will call them A and B. One can define vectors connecting an atom A with its nearest neighbours on sublattice B as

$$\delta_1 = a_0(1,0), \quad \delta_2 = \frac{a_0}{2}(-1,\sqrt{3}), \quad \delta_3 = \frac{a_0}{2}(-1, -\sqrt{3}). \quad (2.1)$$

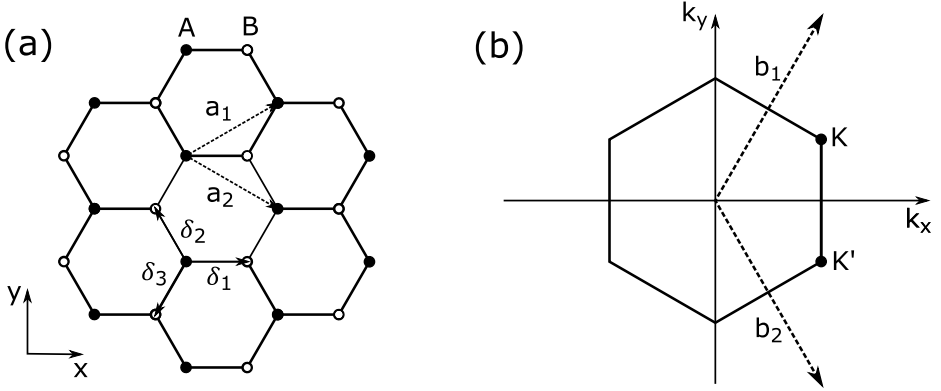


Figure 2.1: (a) Honeycomb graphene lattice with two inequivalent sublattices A and B, showing nearest neighbour vectors δ and primitive lattice vectors \mathbf{a} . (b) Reciprocal space showing the first Brillouin zone, its lattice vectors \mathbf{b} and Dirac points K and K'.

To generate a single triangular sublattice we can use primitive vectors

$$\mathbf{a}_1 = \frac{a_0}{2}(3, \sqrt{3}), \quad \mathbf{a}_2 = \frac{a_0}{2}(3, -\sqrt{3}) \quad (2.2)$$

We can also construct a reciprocal lattice using its primitive vectors

$$\mathbf{b}_1 = \frac{2\pi}{3a_0}(1, \sqrt{3}), \quad \mathbf{b}_2 = \frac{2\pi}{3a_0}(1, -\sqrt{3}) \quad (2.3)$$

Of particular importance are corners of the first Brillouin zone, see Fig. 2.1 (b), with two inequivalent points

$$\mathbf{K} = \frac{2\pi}{3a_0}\left(1, \frac{1}{\sqrt{3}}\right), \quad \mathbf{K}' = \frac{2\pi}{3a_0}\left(1, -\frac{1}{\sqrt{3}}\right) \quad (2.4)$$

In the following section we are going to show how the dispersion relation for electrons can be linearized around these points, from which many unusual properties of graphene arise.

2.1.2 Dirac Hamiltonian

As derived in App. A, the eigenenergies of the honeycomb carbon lattice Hamiltonian form two bands

$$E(\mathbf{k}) = \pm t \left| 1 + e^{-i\mathbf{k}\cdot\mathbf{a}_1} + e^{-i\mathbf{k}\cdot\mathbf{a}_2} \right|, \quad (2.5)$$

where $t \sim 3$ eV is the nearest-neighbour hopping energy for electrons in π bands [29]. Taking the absolute modulus results in

$$E(\mathbf{k}) = \pm t \sqrt{3 + f(\mathbf{k})}, \quad (2.6)$$

where $f(\mathbf{k}) = 2 \cos(\sqrt{3}k_y a_0) + 4 \cos(\frac{3}{2}k_x a_0) \cos(\frac{\sqrt{3}}{2}k_y a_0)$. It is interesting to note that band structure calculations for graphene were available more than half a century before the experimental extraction [1], and including the second nearest-neighbour hopping the bands look like

$$E(\mathbf{k}) = \pm t \sqrt{3 + f(\mathbf{k})} - t' f(\mathbf{k}), \quad (2.7)$$

where the second nearest-neighbour hopping strength is $t' \sim 0.1$ eV [30]. It is worth noting that presence of this correction destroys conduction ($E > 0$) and valence ($E < 0$) band symmetry with respect to each other around $E = 0$. However, since $t' \ll t$ and we will focus on low-energy properties, the second nearest-neighbour correction will be neglected throughout the thesis. Not only the conduction and valence bands are symmetric with respect to each other, they also touch at $E = 0$ at Dirac points from (2.4), see Fig. 2.2. Since for every Carbon atom there is only one π electron participating in π bond formation, while it can accommodate two electrons due to spin degeneracy, the Fermi energy of ideal pristine graphene lies exactly at $E = 0$.

Using the fact that energy is exactly zero at Dirac points, we can expand (A.7) for low energies, or, equivalently, low momentum κ with respect to points K and K', $\mathbf{k} = \mathbf{K} + \boldsymbol{\kappa}$, $\kappa \ll K$, giving us

$$E_{\lambda, \nu}(\boldsymbol{\kappa}) = \lambda \frac{3a_0 t}{2} |\nu \kappa_x - i \kappa_y| = \lambda \hbar v_F \kappa, \quad (2.8)$$

where λ is the energy band index, + for electrons and - for holes, while ν is the Dirac cone index, + for K valley and - for K', and we defined Fermi velocity in graphene $v_f = \frac{3a_0 t}{2\hbar} \sim 10^6$ m/s. Equivalently, we can expand the Hamiltonian relation to the hopping parameter (A.8), giving

$$H_\nu = \hbar v_F \begin{pmatrix} 0 & \nu \kappa_x - i \kappa_y \\ \nu \kappa_x + i \kappa_y & 0 \end{pmatrix}. \quad (2.9)$$

Recalling that $\boldsymbol{\kappa} = -i \nabla$ one arrives at expression

$$H_+ = -i \hbar v_F (\boldsymbol{\sigma} \cdot \nabla), \quad H_- = i \hbar v_F (\boldsymbol{\sigma}^* \cdot \nabla), \quad (2.10)$$

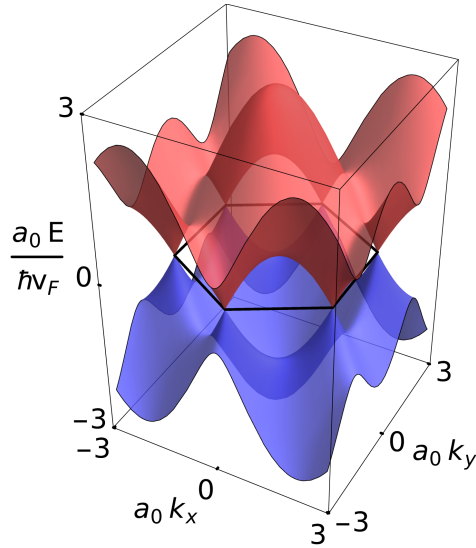


Figure 2.2: Energy bands of graphene. The edges of the first Brillouin zone are shown with a solid black line. At its corners, Dirac points K and K' , conduction and valence bands touch at $E = 0$.

where $\boldsymbol{\sigma} = (\sigma_x, \sigma_y)$ is the Pauli matrix vector in two dimensions. The corresponding eigenvectors are given by

$$\psi_\nu = \frac{1}{\sqrt{2}} \begin{pmatrix} 1 \\ \frac{\nu\kappa_x + i\kappa_y}{\kappa} \end{pmatrix} \quad (2.11)$$

The low-energy dispersion relation (2.8) is linear in momentum and does not depend on electron mass. It can be seen in Fig. 2.2 as cones emerging from K points. This type of dispersion relation is characteristic for relativistic particles, although here the role of speed of light is played by Fermi velocity. Due to this similarity we refer to all these quantities as Dirac Hamiltonian, points, cones, etc. For fused benzene rings the HOMO-LUMO energy gap decreases with increasing the number of rings due to degeneracy of each separate ring, thus if we view graphene as an infinite limit of this case, it is quite intuitive that a continuum of former progressively lower LUMO states, a valence band, touches the conduction band. This simple analogy can be successfully extended to similar 2D materials, e.g. silicene and germanene - they also display zero band gap [11].

Here we should note, that the linearization procedure above imposes limitations on the scales we operate on. We have to assume that electron wavelength is larger than C-C bond distance, so that we are treating graphene as a continuum medium rather than a lattice of discrete sites. Nevertheless, the contributions from the sublattices are still distinguishable. Thus, we describe it as an internal degree of freedom, chirality, since it is similar in mathematical description to the chirality of spin, but here it is due to pseudospinor (2.11) having components on both A (top) and B (bottom) sublattices. We also should note that we have written Hamiltonians for K and K' cones, implying that we neglect any intervalley scattering. So what does the assumption about non-intermixing valleys mean? We have to assume that the potential cannot scatter the particles by a large enough wave vector to bring them from one K valley to another. Since this is done in k -space, in real space it would mean that the potential is smooth on the atomic scale thus covering both types of sublattices. In addition, our sample of graphene should be large on the mesoscopic scale since quantization due to standing waves can mix the valleys together and open up a band gap [31]. In the most general case of intervalley scattering, we have to deal with a four-by-four Hamiltonian matrix and the pseudospinor eigenvectors thus have four components. The real spin degree of freedom enters trivially, since we do not include magnetic field and spin-orbit interaction in our model.

2.2 Fabrication

Graphene, inherently being atomically flat, has long been considered unrealistic. Mere existence of another dimension allows for a multitude of relaxation processes in the direction perpendicular to the hypothetical graphene plane. Thus fluctuations, e.g. in temperature, were deemed to destroy the long-range ordering in two dimensions making the lattice unstable [32, 33]. But it was not until the experimental isolation of graphene in 2004 [3], which brought Geim and Novoselov the Nobel Prize in Physics in 2010, when the final word in the debate has been said. Graphene can be treated as purely two-dimensional to a good degree of approximation, but indeed deviations from a perfect planar structure exist in the form of bulging and curling at the edges [34]. Several fabrication methods have been developed over the years, the main directions being exfoliation, chemical vapour deposition and epitaxial growth of graphene [35].

The original "Scotch tape" method of Novoselov *et. al* [3] is based on micromechanical exfoliation of graphene from graphite. The latter is known to have crystallographic structure consisting of graphene planes weakly bound by interplanar van der Waals forces [36]. The method capitalises on it by attaching an adhesive material to graphite effectively overcoming the van der Waals forces and stripping multiple layers of graphene from the original structure. Applied iteratively, it eventually leads to a single graphene layer being isolated. The strength of this method lies in the simplicity of the setup, and high-quality samples with area up to $2000 \mu\text{m}^2$ [37] are now readily obtainable, thus boosting fundamental graphene research in the labs around the world. The quality of exfoliated graphene flakes is high enough for experimental observation of such exotic phenomena as fractional quantum Hall effect [38] and ballistic transport [39]. Several other variations of the exfoliation process have been developed since the mechanical exfoliation is not scalable to industrial standards [35]. Liquid-phase exfoliation involves solution of graphite or graphite oxide in a liquid [40–42]. This method relies on hydrodynamic forces are to separate the layers. Separation in the liquid phase is commonly done via ultrasonication [40, 43, 44] or stirring and shaking [45, 46]. The disadvantage of using pristine graphite in liquid phase exfoliation is that it usually results in very low yield [40, 47]. As a way to overcome this limitation, graphite oxide is often used as a precursor material instead [48]. Oxidation and chemical intercalation [49, 50] increase the distance between graphene planes in graphite thus decreasing the van der Waals forces and facilitating exfoliation. In addition, graphite oxide, in contrast to graphite, is hydrophilic, which helps to separate layers from each other in liquid. Exfoliated graphite oxide monolayers are then reduced to graphene. However, due to the invasive nature of chemical methods, the resulting graphene is often with a number of defects in the crystal lattice and is generally of lower quality than in micromechanically exfoliated samples [51]. Another alternative is thermal exfoliation. Gas pressure between graphene layers is used to facilitate peeling [52]. The method therefore utilizes graphite oxide or its other functionalized derivatives, or intercalated graphite compounds as precursor materials. It is generally faster than mechanical exfoliation (at high temperatures) [53] and is done in gaseous environments, thus avoiding some culprits of liquid solutions.

Chemical vapor deposition (CVD) uses carbon-containing gas (e.g. methane) flown over typically a metallic (e.g. copper) substrate [54],

heated to a high temperature, that acts as a catalyst for decomposition of the gas. Carbon atoms remain on the metallic surface and graphene islands grow around the initial nucleation centres. The growth process is very sensitive to the type of gaseous precursor used, variations in gas pressure and temperature. Lack of precise control over the parameters results in CVD samples having many grain boundaries between the nucleation domains with different crystalline orientation. Substrate defects and particle contamination are also of concern in this growth mechanism. Low-pressure CVD is therefore used for production of higher-quality films [55]. Millimetre-size grains have been achieved so far [54, 56]. Another issue is related to transfer of graphene from a metallic substrate to an insulating one for electronic applications. In this regard encapsulation in hexagonal boron nitride has been gaining ground [57, 58].

Thermal decomposition of silicon carbide is yet another method to produce graphene [59–61]. SiC substrate is heated to ~ 1200 °C when sublimation of silicon atoms from the surface occurs, leaving behind carbon atoms that form a honeycomb lattice. Si-terminated face reportedly provides better control over the thickness and uniformity of produced graphene. As the monolayer graphene develops on top of the substrate, a so-called "buffer layer" of carbon atoms forms underneath it [62]. It is still strongly bound to SiC and generally does not display electrical properties characteristic for graphene, although shares the same honeycomb lattice. Due to interaction between the monolayer graphene, the buffer layer and SiC substrate, there is reduced experimental control over certain parameters e.g. carrier density and Fermi level, which can be detrimental to electronic applications [63, 64]. Another drawback is the ten-fold price difference between SiC substrates and conventional Si wafers [65]. The direct advantage of this method is that graphene is grown directly on a semi-insulating SiC thus requiring no transfer to another substrate unlike the case for CVD graphene on metals.

In summary, let us discuss possible applications of graphene from aforementioned synthesis processes. Exfoliated graphene is best used in fundamental research and applications where precise control over the layer structure is not crucial. Such applications include composites, where presence of functional groups is beneficial [49], and in transparent conducting films for photovoltaics [66, 67]. CVD-grown graphene is attractive due to potential cheapness, scalability and flexibility of technology. Transfer to different substrates allows applications in flexible electronics, photovoltaics

and field-effect transistors [68]. Epitaxial growth on SiC results in expensive but high-quality samples. It is not suitable for transistors or sensors due to the coupling to the buffer layer, but it does not impede it from high-frequency applications [24]. Graphene from SiC is also perfect for the development of the metrological resistance standard [69, 70]. Production of graphene is of course only one step towards the actual device applications, and in the next section we describe the motivation behind building transistors out of it.

2.3 Graphene FET

A transistor is an essential building block of virtually all modern electronic devices. The ability to mass-produce miniaturized transistors together with falling costs per individual transistor were behind the computerization revolution of the 21st century. In this thesis we focus on a graphene-based field-effect transistor (FET), a device that uses an electric field to control its output. For the setup we discuss in the thesis the device uses four terminals, as shown in Fig. 1 of Paper I. Two contacts, the source (S) and the drain (D) work as charge reservoirs and are used to inject and collect electrons from graphene, which serves as the channel medium. The other two contacts are gates, they control transport of the injected charge carriers through the device. A back gate electrode moves the Fermi level of the graphene sheet up and down the Dirac cone in the channel region connecting the source and the drain. A top gate is used to apply a control signal to a small region in between the source and the drain. Operation of a typical FET depends on the modulation of the conductivity in the channel as a function of the signal applied to the top gate. The first main application of the transistor is as a switch. Its "on" (high source-drain current) and "off" states can be used in digital logic to construct gates and from them more complicated circuitry. The other usage is as an amplifier for signal processing, communication, etc.

The most frequently used benchmark for material performance in transistors is electron mobility μ , which sets the drift velocity of electrons under an external electric field

$$v_d = \mu E. \quad (2.12)$$

Devices with faster operation require smaller size or higher drift velocity and therefore higher mobility. FETs operation deteriorates due to so-called short channel effects [71, 72], which are predicted to be less detrimental

for higher ratio of device length to the thickness of the channel. Potential appeal of graphene is that it has both high intrinsic carrier mobility [73, 74] and the thinnest possible channel length since it is only one atom thick. Typical silicon-based FET technology channel has variation of thickness throughout the device for overall thickness of a few nanometers [75], which degrades the mobility. And that is still 10 times thicker than what graphene technology potentially allows.

However, there is an important drawback for application of GFETs in logical circuits. Typical device operation requires transistors to be switched to the "off" state with no current passing through it. This is achieved by moving the channel into the band gap of a semiconductor, which is typically on the order of 1 eV. Graphene has no band gap, thus increasing dramatically power consumption of a hypothetical GFET-based device. Some effort has been put into altering graphene band structure to open up a band gap in it by using narrow nanoribbons [76, 77], inducing strain [78], applying bias to two different layers in bilayer graphene [79], or through interaction with the substrate material [80]. However, opening of a band gap destroys linear spectrum and turns it into a parabolic one, thus increasing the effective mass of charge carriers and decreasing the mobility. In addition, the mobility in general goes down with increasing of the band gap, and projected graphene device operation is therefore subpar compared to the existing semiconductor technology [81–83]. Research into other 2D materials, which naturally have a band gap, e.g. MoS₂ is quite possibly a better direction [84, 85].

Fortunately, intergrated circuit logic is not the only area where electronic devices are used. There are radiofrequency (RF) applications that do not require the "off" state of the transistor, thus allowing utilization of the strong side of GFETs. A typical RF device operation superimposes a small time-dependent gate signal on top of a dc operating point. The small variation changes the number of carriers in the channel and therefore the drain current. For high-frequency applications, where the gate length is short, mobility stops being the most important device characteristics, since it is used to describe transport under low electric field. The figure of merit for high-field transport is saturation velocity of charge carriers, which is caused primarily by optical phonons, which increase scattering rates of electrons at high energies. It is reportedly several times higher than that of conventional semiconductors [86]. Other figures include the cutoff frequency f_T , at which a short-circuit gain is unity, and which de-

defines the highest possible operational frequency of the transistor. Graphene devices are performing well in comparison with state-of-the-art semiconductor technology [87]. Another important parameter is the maximum oscillation frequency f_{max} , at which the transistor can still amplify power of the small signal. Here graphene devices are lagging behind the semiconductor competitors, but one of the arguments is that this parameter depends strongly on the circuitry the device is connected to, and that part has not been as optimized for graphene as the well-established Si-based technology [88]. Therefore, nowadays a big effort is dedicated to minimization of parasitic resistances, capacitances, etc. present in electrical circuits [89].

There is one more area, where GFETs have a clear advantage compared to the traditional technology - flexible and printable electronics. The obvious drawback of traditionally used semiconductors is that the devices are rigid, so they simply cannot be used here. Until recently, the area has been dominated by organic semiconductors, which typically have mobilities several orders of magnitude lower than those of various graphene setups, see Fig. 8 in a comprehensive review by F. Schwierz [88].

One has to keep in mind that traditional FET theory has been developed for diffusive transport, while the aim of this thesis is to explore ballistic properties of electrons in graphene. Hopefully, the overview presented in this section leaves the reader with a picture of the current state in manufacturing and applications of graphene-based devices, while our goal in the rest of the thesis is to present a theory behind new operational principles that might not have been available or exhausted in the conventional semiconductor technology.

Chapter 3

Quantum tunnelling

In this chapter we examine quantum-mechanical processes that influence transport of electrons through a constant potential landscape. We compare behaviour of the solutions to both Schrödinger and Dirac equations, covering Fabry-Pérot interference, tunnelling through single and double rectangular barrier structures, Klein tunnelling and bound state formation in quantum wells.

3.1 Single barrier tunnelling

In the thesis we work with a two-dimensional system. We assume that one of the dimensions (y) is large enough to disregard any finite-size effects and use translational invariance along this dimension. Thus Schrödinger and Dirac equations written down in this chapter are to be solved only in x coordinate, making it a quasi-1D problem. For this approximation to work, we require the wavelength of the particle to be larger than the possible imperfections of the potential barriers involved in the picture. In this case, the Fermi wavelength should be larger than the defect size, see Fig. 3.1. The potential barriers are assumed to be sharp on the Fermi wavelength scale, while they are smooth on the atomic scale, $a_0 \ll \Delta D \ll \lambda_F$. If this holds, then we can safely assume specular reflection, conserving transverse momentum, for the low-energy particles within the Dirac cone. Assuming the top gate in our transistor setup to be sharp on the electron wavelength scale, we can develop a minimal model of the electrodes connected to a FET transistor using step potentials. We will start with a material with quadratic dispersion relation, e.g. a two-dimensional electron gas (2DEG)

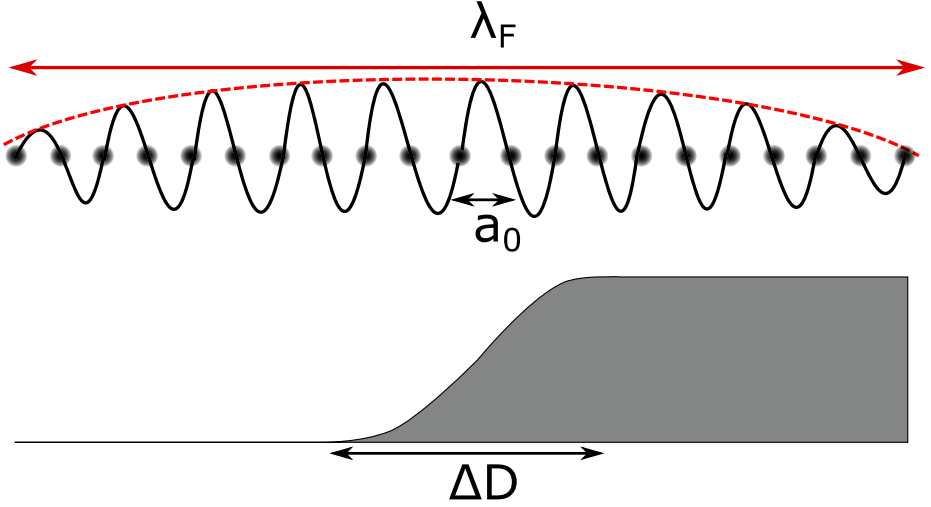


Figure 3.1: The separable length scales: the Fermi wavelength λ_F defines an envelope of a fast oscillating function on the Bloch scale a_0 , while the potential variation scale ΔD is between them $a_0 \ll \Delta D \ll \lambda_F$.

that is commonly used in semiconducting transistors.

3.1.1 Non-relativistic tunnelling

Let us start with a textbook problem of a particle (with energy E and transverse momentum k_y) tunnelling through a rectangular barrier, shown in Fig. 3.2 (a). The time-dependent Schrödinger equation's,

$$\left\{ -\frac{\hbar^2}{2m} \nabla^2 + U_0 [\theta(x) - \theta(x - D)] \right\} \Psi(x, y, t) = i\hbar \frac{\partial}{\partial t} \Psi(x, y, t), \quad (3.1)$$

solution is easily factorized into a spatial and temporal part $\Psi(x, y, t) = \psi(x) e^{ik_y y} e^{-iEt/\hbar}$ since the Hamiltonian is time-independent. We introduce an ansatz

$$\psi(x) = \begin{cases} \frac{1}{\sqrt{2k}} [e^{ikx} + r e^{-ikx}], & x < 0 \\ \frac{1}{\sqrt{2q}} [b e^{iqx} + c e^{-iqx}], & 0 < x < D \\ \frac{1}{\sqrt{2k}} t e^{ikx}, & x > D, \end{cases} \quad (3.2)$$

where $k = \sqrt{\frac{2mE}{\hbar^2} - k_y^2}$ and $q = \sqrt{\frac{2m(E-U_0)}{\hbar^2} - k_y^2}$ are wave vectors in regions with different potentials. Since we are dealing with a second-order

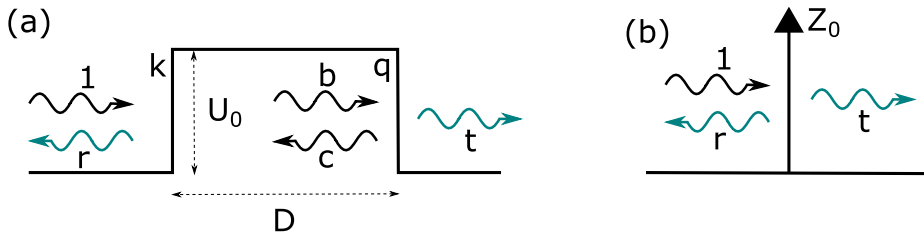


Figure 3.2: (a) Quasi-1D square potential barrier of width D . Wave vectors inside (q) and outside (k) dictate the scattering amplitudes r and t . (b) A corresponding delta barrier.

differential equation and a potential step is finite, we require the wave function and its first derivative to be continuous. Thus plane wave matching at potential interfaces dictates a set of equations

$$\begin{cases} \frac{1}{\sqrt{k}} \begin{bmatrix} 1 \\ k \end{bmatrix} + r \begin{bmatrix} 1 \\ -k \end{bmatrix} = \frac{1}{\sqrt{q}} \left[b \begin{bmatrix} 1 \\ q \end{bmatrix} + c \begin{bmatrix} 1 \\ -q \end{bmatrix} \right] \\ \frac{1}{\sqrt{k}} t \begin{bmatrix} 1 \\ k \end{bmatrix} e^{ikD} = \frac{1}{\sqrt{q}} \left[b \begin{bmatrix} 1 \\ q \end{bmatrix} e^{iqD} + c \begin{bmatrix} 1 \\ -q \end{bmatrix} e^{-iqD} \right], \end{cases} \quad (3.3)$$

Here we should note that we wrote the equations above in a spinor-like form to highlight the similarity in the equation structure with the analogous problem for Dirac electrons, discussed in the next section. In reality the top of these spinors corresponds to the wave function matching, while the bottom to its derivative.

Solutions to this set of equations are given by [90]

$$t = \frac{4kqe^{i(q-k)D}}{(k+q)^2 - (k-q)^2 e^{2iqD}}; \quad r = \frac{(k^2 - q^2) \sin qD}{2ikq \cos qD + (k^2 + q^2) \sin qD}. \quad (3.4)$$

The transmission probability $T = |t|^2$ is shown in Fig. 3.3 (a,b). In the figures we use the angle of incidence φ as a variable, setting a certain transverse momentum $k_y = k \tan \varphi$. We can see that the transmission is exponentially small in the classically forbidden region $E < U_0$, while for high energies it approaches the classical limit of unity. Quantum interference inside the barrier for $E > U_0$ results in a series of fringes in the transmission probability. Throughout the thesis we will refer to the generated pattern as Fabry-Pérot fringes due to similarity with this optical analogue. The interference pattern is the result of scattering off two

partially reflecting surfaces, in our case boundaries between regions with different potentials. If we examine (3.4) more closely, we can easily see that for real wave vectors ($E > U_0$) the interference term is dictated by e^{2iqD} , which is the wave function phase accumulated over one round trip inside the barrier. In fact, the reflection amplitude vanishes for $\sin qD = 0$, therefore defining maxima positions in Fig. 3.3 (b) at $E = U_0 + (n\hbar\pi)^2/(2mD^2)$ for integer n . Thus the interference pattern depends on the width of the barrier and the energy of the particle. The quadratic dispersion relation of particles manifests itself in the angular dependence of the fringes in panel (a). More on this subject is given in Section 3.2.

After examining the tunnelling picture of a rectangular barrier, we can look at its delta-potential approximation by taking the limit $D \rightarrow 0$ while keeping $U_0D = \frac{\hbar^2 Z_0}{2m}$ constant. The width of the barrier becomes infinitesimally small, while its height infinitely high, see Fig. 3.2(b), resulting in the Schrödinger equation (3.1) assuming the form

$$\frac{\hbar^2}{2m} \left[-\nabla^2 + Z_0\delta(x) \right] \psi(x) = E\psi(x) \quad (3.5)$$

after separation of variables. One can integrate it directly to derive a suitable boundary condition or follow a limiting procedure, both of which lead to the same result as shown in App. B.1. The transmission amplitude is then given by

$$t = \frac{1}{1 + \frac{iZ_0}{2k}} \quad (3.6)$$

With the potential width and height merged into one parameter, Z_0 defines the only energy scale remaining, see Fig. 3.3 (b,d). As a result, the Fabry-Pérot fringes disappear from the picture, compared to the rectangular barrier. Since the goal of the thesis is considering graphene-based devices, we will now derive the corresponding expressions for tunnelling of relativistic particles and compare it to the case examined in this section. The reason to introduce the delta potential approximation is that the Fermi wavelength of electrons in graphene is large, and a narrow top gate region can be then effectively modelled as having vanishing width. We should note that since the height of a square barrier is bounded from above by being within the Dirac cone (roughly the hopping strength of 3 eV), it sets an upper bound on the delta barrier strength $Z_0 \ll \frac{3eV}{|E-U_C|}$, but for operation close to the charge neutrality point of graphene it can be made arbitrarily large.

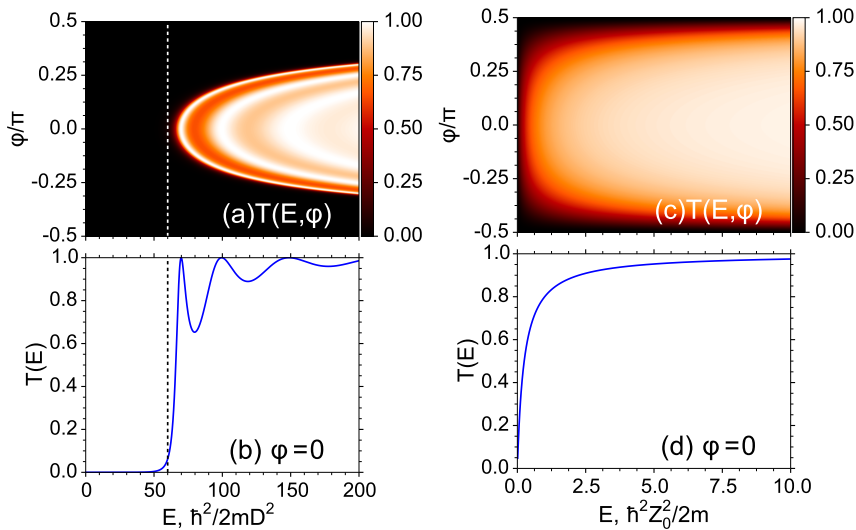


Figure 3.3: (a) Transmission through a 2D rectangular barrier in Schrödinger equation as a function of incidence energy and angle and (b) its cross section at $\varphi = 0$. Dashed line indicates the height of potential step U_0 . (c) and (d) display corresponding figures for a delta barrier of strength Z_0 .

3.1.2 Klein tunnelling

Adding a rectangular barrier to the effective low-energy Dirac Hamiltonian derived in Chapter 2 gives

$$\{-i\hbar v_F \boldsymbol{\sigma} \cdot \nabla + U_0 [\theta(x) - \theta(x - D)]\} \Psi(x, y, t) = i\hbar \frac{\partial}{\partial t} \Psi(x, y, t) \quad (3.7)$$

Plane wave matching is done as in the previous section, but for solutions of the Dirac equation (here in K valley of graphene) require continuity of the wave function, both of its pseudospinor components. Unlike Schrödinger equation, it is a first-order differential equation, therefore there is no requirement on the first derivative of the wave function. Despite this difference, the boundary condition results in a very similar expression

$$\begin{cases} \frac{1}{\sqrt{2v}} \left[\begin{pmatrix} 1 \\ \eta \end{pmatrix} + r \begin{pmatrix} 1 \\ \bar{\eta} \end{pmatrix} \right] = \frac{1}{\sqrt{2w}} \left[b \begin{pmatrix} 1 \\ \mu \end{pmatrix} + c \begin{pmatrix} 1 \\ \bar{\mu} \end{pmatrix} \right] \\ \frac{1}{\sqrt{2v}} t \begin{pmatrix} 1 \\ \eta \end{pmatrix} e^{ikD} = \frac{1}{\sqrt{2w}} \left[b \begin{pmatrix} 1 \\ \mu \end{pmatrix} e^{iqD} + c \begin{pmatrix} 1 \\ \bar{\mu} \end{pmatrix} e^{-iqD} \right]. \end{cases} \quad (3.8)$$

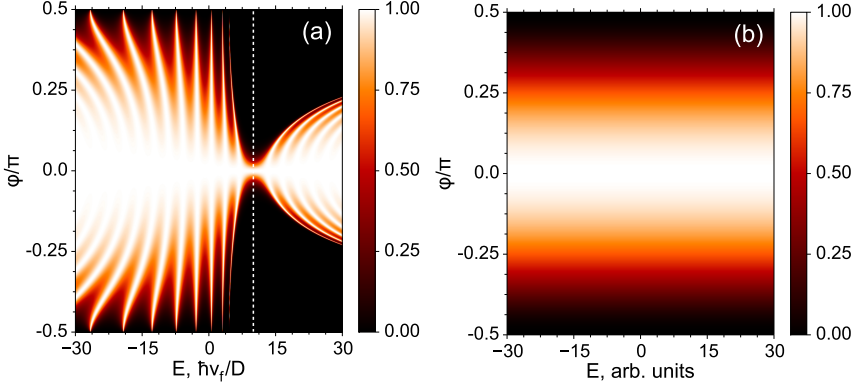


Figure 3.4: (a) Transmission through a 2D rectangular barrier for Dirac particles as a function of incidence energy and angle, the barrier height is indicated by the dashed line, and (b) corresponding transmission through a delta barrier of strength $Z_0 = 0.4\pi$.

The spinor components are given by

$$\begin{aligned}\eta &= \frac{k + ik_y}{E}, & \bar{\eta} &= \frac{-k + ik_y}{E}, \\ k &= \text{sgn}(E)\sqrt{E^2 - k_y^2}, \\ \mu &= \frac{q + ik_y}{E}, & \bar{\mu} &= \frac{-q + ik_y}{E} \\ q &= \text{sgn}(E - U_0)\sqrt{(E - U_0)^2 - k_y^2},\end{aligned}$$

where we have put $\hbar = 1$ and $v_F = 1$ so that we use energy E instead of wave vector modulus. Here we should also note that the probability flux in graphene is given by

$$j = \psi^\dagger \sigma_x \psi, \quad (3.9)$$

and normalizing it to unity gives us

$$v = \frac{k}{E} \quad \text{and} \quad w = \frac{q}{E - U_0}. \quad (3.10)$$

By comparing (3.8) and (C.7) we notice that the difference comes in the second line in pseudospinors: in the quadratic case it is a wave vector component along x axis, while in the massless relativistic case for propagating waves it is just a phase $e^{i\varphi}$ dependent on the angle of incidence

$\varphi = \sin^{-1}(k_y/E)$. Solving (3.8) for the transmission coefficient gives

$$t = \frac{(\eta - \bar{\eta})(\mu - \bar{\mu})e^{i(q-k)D}}{(\eta - \bar{\mu})(\mu - \bar{\eta}) - (\eta - \mu)(\bar{\mu} - \bar{\eta})e^{2iqD}}. \quad (3.11)$$

Although the form of the solution looks similar to that in the quadratic dispersion case, having spinor components rather than wave vectors makes a dramatic difference, as visualized in Fig. 3.4. For normal incidence $\varphi = 0$, all pseudospinors align $\eta = \mu = 1$, $\bar{\eta} = \bar{\mu} = -1$. Plugging it into (3.11) it is clear that the transmission probability becomes $T = |t|^2 = 1$ meaning that the barrier is completely transparent to Dirac particles at normal incidence, irrespective of their energy, barrier height or width. This phenomenon is known as Klein paradox, after the discovery made by Oskar Klein in 1929 [91] in connection to tunnelling of relativistic particles through a 1D potential step. The original formulation of the paradox attracted a lot of attention at the time and was shown to be closely linked to supercritical positron production in heavy nuclei, particle-antiparticle pair creation at the black hole horizon and interband tunnelling in semiconductors [92, 93]. One explanation of the "paradox" is that the group velocity of Dirac electrons is the same as their phase velocity due to the linear dispersion relation. Thus waves of any shape have to travel undistorted.

Similarly to the non-relativistic case, there is a region in parameter space (E, φ) , where the waves are evanescent inside the barrier, namely for angles larger than the critical value

$$|\varphi| > \phi = \sin^{-1} \left| \frac{E - U_0}{E} \right|. \quad (3.12)$$

Unlike the non-relativistic waves, which are evanescent for energies below the barrier height, such region in graphene is concentrated around the point close to the potential height $E = U_0$, as is clearly seen in Fig. 3.4 (a). In both cases we can view the potential as shifting the corresponding dispersion relation $E(k, k_y)$ along the energy axis. But in the usual quadratic case $E \propto (k^2 + k_y^2)$ we have a band bottom $E = 0$ below which there are no allowed states since wave vectors become imaginary, while for graphene there is only a single point, $E = U_0$ where there are no propagating states allowed. Ambipolarity of graphene's spectrum has been used in e.g. frequency doublers [94].

In addition to Klein tunnelling and evanescent region, there is Fabry-Pérot interference similar to that discussed for non-relativistic particles,

except charge carriers in graphene show the pattern at all energies due to ambipolarity of the Dirac cone. The asymmetry in the picture around $E = U_0$ is due to the barrier having a certain sign $U_0 > 0$, the picture is mirrored around this point if we take $U_0 \rightarrow -U_0$.

Now we can look at the delta-barrier approximation of the rectangular potential in graphene, the result of which has been used in the appended Papers. Using the correct limiting procedure (see App. B.2) one obtains the transmission amplitude as

$$t = \frac{\eta - \bar{\eta}}{(\eta - \bar{\eta}) \cos Z_0 + 2i \sin Z_0} = \frac{\cos \varphi}{\cos \varphi \cos Z_0 + i \sin Z_0}. \quad (3.13)$$

If now compare the transmission probability, shown in Fig. 3.4 (b), to that of the rectangular barrier, we notice that the energy scale disappears from the picture completely. For an infinitely high barrier, particles tunnel through it freely at perpendicular incidence, but also the characteristic scale $\hbar v_f/D \rightarrow \infty$ disappears, thus no Fabry-Pérot interference is observed.

3.1.3 Pseudospin matching

In this section we will show a complementary picture to the phase velocity explanation given above. Since for the electronic wave function in graphene we require its continuity at the interfaces of a finite potential barrier, the transmitted and reflected wave amplitudes essentially depend on how well the pseudospinors match and can nicely be represented graphically, see Fig. 3.5. Scattering amplitudes through a single interface (a potential step) in panel (a) are given by

$$t = \sqrt{\frac{w}{v}} \frac{\eta - \bar{\eta}}{\mu - \bar{\eta}} \quad \text{and} \quad r = \frac{\eta - \mu}{\mu - \bar{\eta}}. \quad (3.14)$$

Since the transverse momentum is conserved, the wave vectors of incoming and reflected wave lie on the same circle, which is a cross section of the Dirac cone at energy E , while the transmitted wave at $E - U_0$ is not aligned perfectly with the incoming wave unless $k = q$, which is possible only in the absence of the potential step in this case. Addition of the second scattering interface as in the previous section allows the transmitted wave to have the same wave vector as the incident one, thus potentially allowing perfect transmission (displayed by Fabry-Pérot resonances or Klein tunnelling). Note also that for certain values of k_y , only states in the bigger circle

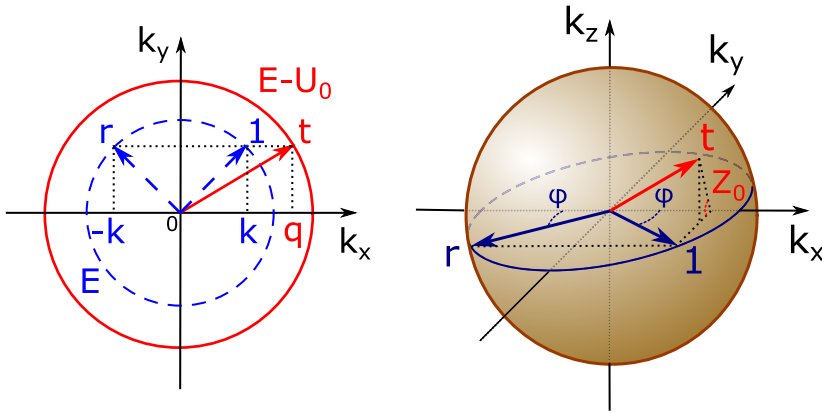


Figure 3.5: (a) Pseudospin mismatch at a potential step results in reduced transmission. (b) Delta barrier rotates transmitted pseudospin around k_x on a Bloch sphere, also resulting in a mismatch. 1, r and t are amplitudes associated with wave vectors of the incoming, reflected and transmitted wave, respectively.

exist, which is exactly what defines the critical angle for evanescent waves discussed above.

Fig. 3.5 (b) represents a more complicated case of scattering through a delta barrier. Similarly to real spins, we can represent the pseudospinors involved on a unit Bloch sphere. The boundary condition (B.5) implies that the delta barrier acts as a rotation operator $\exp(iZ_0\sigma_x)$, meaning it rotates a pseudospinor it acts on by an angle Z_0 around x axis. That means that it tries to move it out of the Dirac cone plane (k_x, k_y) of the incoming wave. Naturally, it introduces a mismatch in pseudospin and results in a generally non-unitary transmission. Thus solving the boundary condition means finding a combination of complex coefficients r and t such that the resulting pseudospinor lies back in the Dirac cone plane. Here we note that understanding Z_0 as a rotation angle also easily illustrates periodicity of the transmission amplitude with respect to it. The original Fabry-Pérot oscillations of the square barrier do not disappear completely, but rather a single cut across the interference fringe is made for every Z_0 value now. Tuning it between 0 and 2π spans all possible values of transmission between maximum of unity for all angles at $Z_0 = 0$ and minimum at $Z_0 = \pi/2$.

3.2 Bound states

So far we have been talking about the propagating states and transmission through the system. But there is another set of non-vanishing solutions to it in absence of any incoming waves - the so-called bound states.

3.2.1 Non-relativistic wells

Let us revisit the time-independent Schrödinger equation in the presence of a potential

$$\left[-\frac{\hbar^2}{2m} \nabla^2 + U(x) \right] \psi(x) = E\psi(x). \quad (3.15)$$

Returning to the general ansatz of $\psi(x) = Ae^{ikx} + Be^{-ikx}$, we can note that the absence of propagating states means $\lim_{x \rightarrow \pm\infty} \psi(x) = 0$. This immediately tells us that the exponentials have to be real thus the wave vector k has to be imaginary. Recalling the dispersion relation, $E = \frac{\hbar^2(k^2 + k_y^2)}{2m}$ in two dimensions, one realises that the condition for the bound state to exist is that the wave is evanescent outside of the potential region $U(x)$, $E < |k_y|^2$, while it is propagating at least in some part inside of it, $E - U(x) > |k_y|^2$. If one considers $U_0 < 0$ in (3.1) we arrive at a textbook example of a finite-depth potential well. The bound state position can be obtained by solving the non-algebraic equations derived in App. C.1. But here we will instead take a limit of a deep well $U_0 \rightarrow -\infty$, leaving us with the particle-in-a-box standing wave condition

$$\sin(qD) = 0, \quad (3.16)$$

which is exactly the same as the requirement for the Fabry-Pérot interference maxima in the tunnelling picture. So the same constructive interference is responsible for both Fabry-Pérot oscillations for tunnelling above the square barrier $E > U_0 > 0$ and for the bound states in a potential well $0 > E > U_0$. Due to the dispersion relation being quadratic, the bound state energies are not equidistant from each other, thus diminishing chances of simultaneous excitation of multiple bound states by e.g. radiation of certain frequency.

A straightforward way to obtain the bound state condition for the corresponding delta well is by removing the incoming wave in the boundary condition (B.1), while setting $U_0 < 0$ and transforming the wave vector

$k \rightarrow i\kappa, \kappa \in \mathfrak{R}$. Then one arrives at

$$\kappa = -iZ_0/2 \quad \Longrightarrow \quad E = -\frac{\hbar^2 Z_0^2}{8m}, \quad (3.17)$$

thus it can host only a single bound state.

3.2.2 Relativistic wells

We can repeat the procedure of the previous section to find the requirement for a bound state in a potential well in graphene. Due to the continuity of the electron-hole spectrum, any potential in graphene can act as a well for one type of carriers, which distinguishes it from the 2DEG setup. The non-algebraic condition for a square well in graphene (see App. C.2) reads

$$\frac{\kappa + k_y}{E} \cos(qD - \theta) - \frac{-\kappa + k_y}{E} \cos(qD + \theta) + \sin(qD) = 0, \quad (3.18)$$

where $\theta = \tan^{-1}(k_y/q)$. It is a non-algebraic equation with multiple non-equidistant solutions. For a delta-potential approximation the condition simplifies to

$$k = i\kappa = -iE \tan Z_0, \quad (3.19)$$

again hosting only a single bound state. We should point out that in the setup that we have been describing so far, the bound state is disconnected from a continuum of propagating states, since it requires waves to be evanescent on either side of the barrier. However, it is possible to excite the bound state if we consider k_y conservation and add a more complicated potential structure $U(x)$, as in the double barrier tunnelling setup of the next section. Effects of the scattering through the bound state are the main theme of Papers included in the thesis, with Papers I and II focusing on mechanisms of resonance formation. However, in the papers we discuss operation under a time-dependent gate drive, so before proceeding to that, we need to establish a few more key ideas in the static potential landscape.

3.3 Double barrier tunnelling

Let us consider a system of two barriers shown in Fig. 3.6. We can assume they have different scattering amplitudes: t_1, r_1 and t_2, r_2 , with exact dependence already derived in the previous section. To obtain the total

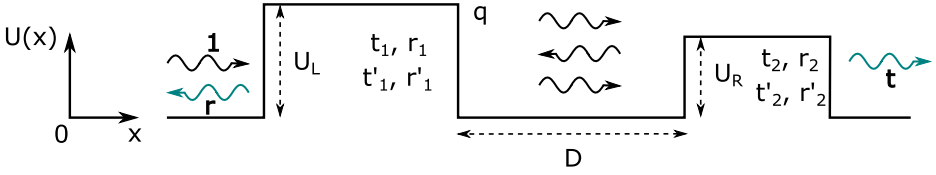


Figure 3.6: Scattering from an asymmetric double barrier. Scattering amplitudes of individual barriers are shown on them.

transmission we can sum over all possible scattering events that lead to it, resulting in an infinite series

$$t = t_1 e^{iqD} (1 + r_2 e^{iqD} r'_1 e^{iqD} + r_2 e^{iqD} r'_1 e^{iqD} r_2 e^{iqD} r'_1 e^{iqD} + \dots) t_2, \quad (3.20)$$

where r' are reflection amplitudes for waves incident from the left onto the barriers. Let us examine this expression term by term. For the particle to be transmitted through the whole system, it has to pass the first barrier with amplitude t_1 , the free propagation region giving the phase e^{iqD} , and the second barrier with amplitude t_2 . However, this excludes any reflection processes from the barriers, so this term is included in the brackets. The wave either goes through directly (1) or reflects from the second barrier (r_2), travels back (e^{iqD}), reflects from the first one (r'_1), and goes forward again (e^{iqD}). This can happen an infinite number of times, and we should sum up all the contributions. For every roundtrip performed by the wave we have to include one more factor of $r_2 e^{iqD} r'_1 e^{iqD}$ inside the sum, producing a geometrical progression. Summing over the geometrical progression therefore gives us

$$t = t_1 e^{iqD} \frac{1}{1 - r'_1 e^{iqD} r_2 e^{iqD}} t_2 \quad (3.21)$$

Just like for the case of tunnelling through a single rectangular barrier, there is an interference term e^{2ikD} responsible for the phase accumulation during free propagation between the scattering interfaces. Calculating the absolute value of the transmission yields:

$$T = \frac{T_1 T_2}{R'_1 R_2 - 2\Re[r'_1 r_2 e^{i2qD}] + 1}. \quad (3.22)$$

For a symmetric double barrier this gives

$$T = \frac{T_1^2}{R_1^2 - 2R_1 \cos(2qD) + 1}. \quad (3.23)$$

One should immediately notice that the transmission becomes unity at the resonance condition $\sin qD = 0$. The condition itself is the same as the Fabry-Pérot requirement for the single barrier, or the bound state for a single quantum well. Here the well is formed by the region between U_L and U_R . What is remarkable about this result is that it actually joins the two possibilities in one potential structure. Since energy E can be both above and below the barrier height(s), both phenomena can be observed as a function of it. The bound state resonances are much more interesting since for $E \ll U_L$ for 2DEG the individual square barriers are virtually opaque with $R_1 \approx 1$. Despite that, constructive interference between the barriers allows the whole structure to be completely transparent on resonances, highlighting the importance of coherent transport.

Assuming zero transverse momentum for simplicity, we can expand $\cos(2qD)$ to the second order in energy around a single bound state E_b as

$$\cos(2qD) = \cos(\alpha\sqrt{E}) = 1 - \frac{1}{2} \frac{\alpha^2}{4E_b} (E - E_b)^2, \quad (3.24)$$

and plug it into the transmission probability giving

$$T = \frac{\Gamma^2}{(E - E_b)^2 + \Gamma^2}, \quad (3.25)$$

with $\Gamma = \frac{2\sqrt{E_b}}{\alpha} \frac{T_1}{\sqrt{R_1}}$. This tells us that the shape of the transmission probability around the resonance is Lorentzian centered at the bound state with broadening Γ depending on the transmission through an individual barrier. For opaque barriers ($T \ll 1$), the resonances are very sharp.

Such multi-barrier systems have been extensively studied for semiconducting heterostructures and found applications e.g. in resonant-tunnelling diodes [95–97]. The pros of using such diodes are that high operational speed is achievable for narrow heterostructures in addition to the small size of it as an advantage by itself. An active area of research is utilizing resonant-tunneling diodes for THz frequency applications [98, 99]. Setups for graphene have also been considered [100, 101].

The discussion in this section so far was quite general, with the result applicable to both 2DEGs and graphene. The first difference comes in how the devices are operated, since in graphene a back gate can be easily used to tune to the correct energy window. Second, the gapless dispersion relation of graphene allows the duality between the potential well and barrier to be explored. We have learned that there is a general problem with electron

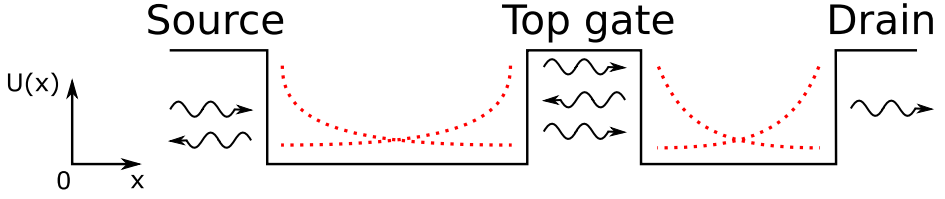


Figure 3.7: Schematics of a double barrier resonant tunnelling in graphene. Evanescent modes are shown as dotted lines.

confinement in graphene due to Klein tunnelling. Indeed, potentials U_L and U_R in Fig. 3.6 appear as transparent barriers for $E \ll U_L$. However, using a back gate we can effectively flip the picture upside down, see Fig. 3.7, which is the setup discussed in Paper II. When metallic electrodes are deposited on graphene, they introduce doping changing the position of the Dirac point with respect to the undoped sample [102, 103]. Similarly to gating, we can model the change in potential using step functions $U(x) = U_L\theta(-x-L_1) + U_0[\theta(x) - \theta(x-D)] + U_R\theta(x-L_2)$. In this setup, we require a particle injected from the left to be propagating in the lead, leaving it with a large transverse momentum $k_y = (E - U_L) \sin \phi$, (angle ϕ is now defined in the lead) for $E \ll U_L$, while it then scatters into a smaller cone cross section in the channel between the source and the top gate, resulting in the imaginary longitudinal momentum component, as was described before. Presence of evanescent modes makes the tunnelling barriers on either side of the top gate opaque, thus we can apply the resonant tunnelling logic from above. Double barrier tunnelling was part of the discussion in Paper II, where we examined its effects on time-dependent transport. It is interesting to note that there are proposals of resonant tunnelling setups rather in the direction perpendicular to the graphene sheet combining it with other 2D materials, resulting in extremely thin heterostructures and potentially leading to fast operational times [104].

Chapter 4

AC field scattering

In this chapter we discuss how interaction with time-periodic electric field influences transport through an otherwise static potential landscape. In particular we show how energy sidebands emerge and discuss possible inelastic processes arising from scattering at an oscillating barrier. We present how such processes results in Fano and Breit-Wigner type resonances after interaction with a quasibound state.

4.1 Tien-Gordon theory.

In our GFET model we have a time-dependent drive $V_1 \cos \Omega t$ applied to the top gate. The easiest way to analyse scattering from a time-dependent potential is to consider solutions to the SE inside of it first. The discussion here will follow the theory developed by Tien and Gordon [105] for microwave-driven superconductor-insulator-superconductor tunnel junctions. As we know, for a spatially homogeneous potential U_0 , time-independent SE provides an energy eigenvalue from solving

$$H_0 \psi(\mathbf{r}) = E \psi(\mathbf{r}), \quad (4.1)$$

where $H_0 = -\frac{\hbar^2}{2m} \nabla^2 + U_0$. Now, once we add an oscillating part to the existing potential, the time-dependent SE takes the form

$$i\hbar \frac{\partial}{\partial t} \Psi(\mathbf{r}, t) = [H_0 + U_1 \cos(\Omega t)] \Psi(\mathbf{r}, t) \quad (4.2)$$

One can now use separation of variables into spatial and temporal components $\Psi(\vec{r}, t) = \psi(\vec{r}) \Phi(t)$ since H_0 is time-independent and the potential

has no space dependence. The resulting partial differential equation for $\Phi(t)$

$$i\hbar \frac{d\Phi(t)}{dt} = [E - U_1 \cos(\Omega t)]\Phi(t) \quad (4.3)$$

can be readily solved as

$$\Phi(t) = \exp\left[-\frac{i}{\hbar}\left(Et - \frac{U_1}{\Omega} \sin \Omega t\right)\right] \quad (4.4)$$

The time dependence in the exponential is non-trivial, and to present it in a more tractable form we will use a Fourier expansion of it

$$\Phi(t) = e^{-iEt/\hbar} \sum_{n=-\infty}^{\infty} c_n \exp[-in\Omega t]. \quad (4.5)$$

The unknown expansion coefficients c_n are found from the inverse Fourier transform as

$$c_n = \frac{1}{2\pi} \int_{-\pi}^{\pi} d(\Omega t) \exp\left[i(n\Omega t - \frac{U_1}{\hbar\Omega} \sin \Omega t)\right], \quad (4.6)$$

but this is nothing else but an integral expression of the n^{th} -order Bessel functions of the first kind $J_n\left(\frac{U_1}{\hbar\Omega}\right)$. In fact, this procedure for exponentials of trigonometric functions is known as the Jacobi–Anger expansion. The spatial distribution is of course not affected by introduction of this time-dependent potential. Therefore, the solutions to the time-dependent SE take the form

$$\Psi(\mathbf{r}, t) = \psi(\mathbf{r}) \sum_{n=-\infty}^{\infty} [J_n(\zeta_1) \exp(-i(E + n\hbar\Omega)t/\hbar)], \quad (4.7)$$

where $\zeta_1 = \frac{U_1}{\hbar\Omega}$. From the physical point of view, each component of the sum represents a solution to a time-independent SE with energy $E + n\hbar\Omega$, thus creating an effective ladder of energy sidebands. One can note that quasienergy E is not uniquely defined in this problem since we did not impose any boundary condition. However, once we look at the scattering problem from such a potential, it is natural to assume E to represent the energy of the particle impinging onto the barrier. In such treatment, $n = 0$ is considered as the main energy band, the one which survives in the absence of the oscillating potential. Waves incident on the barrier can now

absorb or emit multiples of energy quantum $\hbar\Omega$ scattering into different energy states, effectively creating multiple scattering channels instead of a single one as in the static case. Naturally, the overall transmission through such barrier is the sum over all single channel transmissions. The advantage of this theory is that it relies on the separation of variables, which can be done as effectively for the Dirac Hamiltonian, giving the same result. The only difference is that the spatial part of the wave function is represented by pseudospinors.

4.1.1 Bessel functions

The natural questions arising at this point are what is the distribution of amplitudes in the energy expansion and how does the strength of the oscillation affect this distribution. To answer this first we will provide some properties of the Bessel functions:

$$\sum_{n=-\infty}^{\infty} J_n = 1, \quad (4.8)$$

$$\sum_{n=-\infty}^{\infty} J_n^2 = 1, \quad \text{and} \quad (4.9)$$

$$J_{-|n|}(\zeta_1) = (-1)^{|n|} J_{|n|}(\zeta_1). \quad (4.10)$$

The first two will ensure that the total probability is conserved during scattering, while the last one tells us that there is a built-in symmetry in the strength with which sidebands (symmetric around the main energy band) contribute to the total distribution. Having this in mind, we can plot $J_{n \geq 0}(\zeta_1)$, as shown in Fig. 4.1 (a). For $\zeta \ll 1$ all but the main energy band contributions may be neglected, while with increasing the strength of the drive we have to take more Bessel functions and thus sidebands into account. We can represent Bessel functions in terms of a power series

$$J_{n \geq 0}(\zeta_1) = \sum_{l=0}^{\infty} (-1)^l \frac{\left(\frac{\zeta_1}{2}\right)^{2l+n}}{l!(l+n)!}. \quad (4.11)$$

Fig. 4.1 (b) provides a visual cue to what happens to the Bessel functions. For a weak drive $\zeta_1 \ll 2$ the powers in the sum decay quickly with increasing n due to the smallness of parameter, $J_n(\zeta_1 \ll 1) \approx \frac{1}{n!} \left(\frac{\zeta_1}{2}\right)^n$. For the strong drive however, there is a redistribution of "weight" from the main

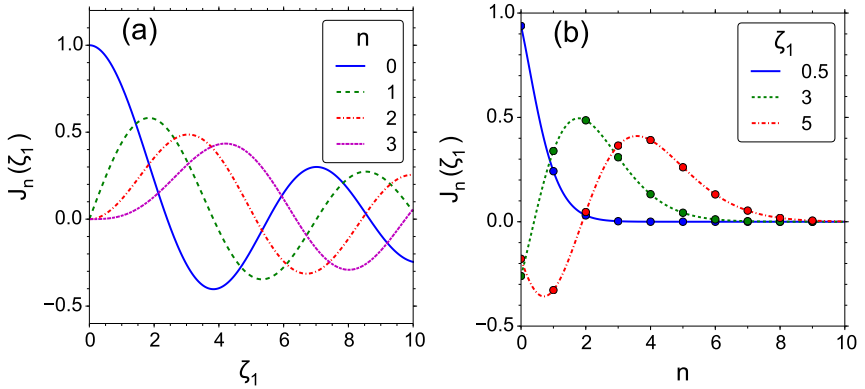


Figure 4.1: (a) Distribution of Bessel functions for different sideband index n as function of the dimensionless oscillating potential strength $\zeta_1 = U_1/\hbar\Omega$, (b) Decay of Bessel functions at high sideband indices. Markers represent integer index values.

energy band to higher index sidebands. In fact, at a very high driving strength,

$$J_n(\zeta_1 \gg n^2) \approx \sqrt{\frac{2}{\pi\zeta_1}} \cos(\zeta_1 - n\pi/2 - \pi/4), \quad (4.12)$$

low index sidebands contribute with approximately the same strength. Nevertheless, for high enough sideband index n all Bessel functions decay to zero due to the factorial scaling in the denominator of the sum, which provides us with an effective cutoff that we can introduce to the sum (4.7) while still maintaining probability conservation to a satisfactory degree. It is interesting how perturbation strength $\zeta_1 = U_1/\hbar\Omega$ depends on both parameters of the AC signal simultaneously. Put in crude words, the driving field strength should be higher than the absorbed/emitted photon energy for such an event to happen. Or, on the other hand, the time given to the system ($1/\Omega$) to react to the perturbation should be long enough or the effect will diminish.

4.2 Oscillating delta-barrier in Schrödinger equation

We will start with a square barrier Hamiltonian from Chapter 3 with an addition of the time-dependent oscillation

$$H(x,t) = -\frac{\hbar^2}{2m}\nabla^2 + (U_0 + U_1 \cos \Omega t) [\theta(x) - \theta(x - D)], \quad (4.13)$$

here we will assume the system is one-dimensional for simplicity. According to Tien-Gordon effect, sidebands are formed in the barrier. It is natural to assume that incident waves can pick up energy quanta upon scattering from the interfaces with it, giving the wave function outside the barrier the form [106]

$$\Psi(x,t) = \begin{cases} \sum_{n=-\infty}^{\infty} [\delta_{n0} e^{ik_n x} + r_n e^{-ik_n x}] e^{-in\Omega t} e^{-iEt/\hbar}, & x < 0 \\ \sum_{n=-\infty}^{\infty} t_n e^{ik_n x} e^{-in\Omega t} e^{-iEt/\hbar}, & x > D \end{cases} \quad (4.14)$$

Here δ_{n0} is Kronecker delta function, so that the incident wave consists only of the main energy band $n = 0$, while reflection r_n and transmission t_n amplitudes are defined for all sidebands with energies $E_n = E + n\hbar\Omega$ and momentum $k_n = \sqrt{2m(E + n\hbar\Omega)}/\hbar$. Inside the barrier, however, multiple reflections may occur, producing

$$\Psi(x,t) = \sum_{n=-\infty}^{\infty} [b_n e^{iq_n x} + c_n e^{-iq_n x}] e^{-in\Omega t} \sum_{m=-\infty}^{\infty} J_m \left(\frac{eV}{\hbar\omega} \right) e^{-i(E+m\hbar\Omega)t/\hbar}, \quad (4.15)$$

where $q_n = \sqrt{2m(E + n\hbar\Omega - U_0)}/\hbar$. Noting that the harmonics $e^{in\Omega t}$ are orthogonal to each other, we rewrite the last equation as

$$\Psi(x,t) = \sum_{n,l=-\infty}^{\infty} [b_n e^{iq_n x} + c_n e^{-iq_n x}] J_{n-l} \left(\frac{eV}{\hbar\omega} \right) e^{-i(E+(n-l)\hbar\Omega)t/\hbar}. \quad (4.16)$$

Continuity of the wave function and its derivative give us the boundary condition

$$\begin{cases} \delta_{n0} \begin{pmatrix} 1 \\ k_n \end{pmatrix} + r_n \begin{pmatrix} 1 \\ -k_n \end{pmatrix} = \sum_{l=-\infty}^{\infty} \left[b_l \begin{pmatrix} 1 \\ q_l \end{pmatrix} + c_l \begin{pmatrix} 1 \\ -q_l \end{pmatrix} \right] J_{n-l} \left(\frac{U_1}{\hbar\Omega} \right) \\ t_n \begin{pmatrix} 1 \\ k_n \end{pmatrix} = \sum_{l=-\infty}^{\infty} \left[b_l \begin{pmatrix} 1 \\ q_l \end{pmatrix} e^{iq_l D} + c_l \begin{pmatrix} 1 \\ -q_l \end{pmatrix} e^{-iq_l D} \right] J_{n-l} \left(\frac{U_1}{\hbar\Omega} \right). \end{cases} \quad (4.17)$$

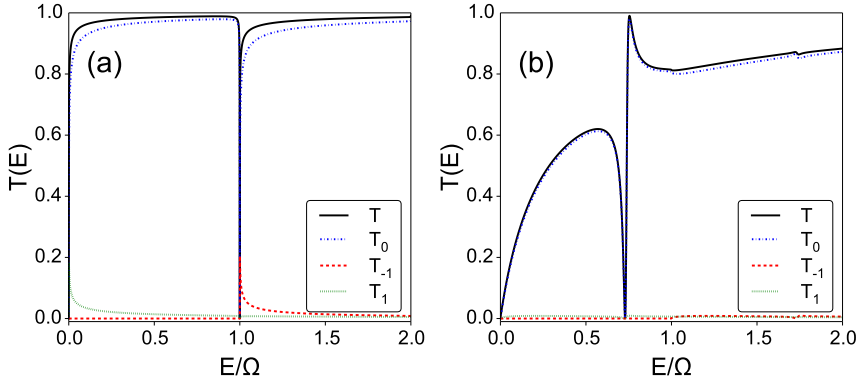


Figure 4.2: Transmission through a weak oscillating delta barrier $Z_1 = 0.45$. (a) The static well is absent, $Z_0 = 0$. Opening of channels causes a resonant dip in the total transmission. (b) The static well of finite depth $Z_0 = -1$ results in a Fano resonance at the bound state energy.

We are interested in how the newly formed channels affect transport through the system. A delta-potential model presents a clearer picture of the processes involved in scattering. Similarly to what we have done in Chapter 3 for the static barrier, we can derive a boundary condition for the dynamic case, see App. B.3. The resulting equation for transmission amplitudes can be written in the matrix form

$$\check{A}\mathbf{t} = \boldsymbol{\delta}, \quad (4.18)$$

where \mathbf{t} is a vector of all harmonics (in the sideband space) $\mathbf{t}_n = t_n$ and the incoming wave gives $\boldsymbol{\delta}_n = \delta_{n0}$, while the matrix

$$\check{A}_{mn} = \left(1 + \frac{iZ_0}{2k_n}\right)\delta_{|m-n|,0} + \frac{iZ_1}{4k_n}\delta_{|m-n|,1} \quad (4.19)$$

in the sideband space is tridiagonal. We note that we have not used normalization of the probability flux to unity, thus the transmission through the system in the n^{th} channel is given by $T_n = |t_n|^2 \frac{k_n}{k_0}$. The equation set can be solved numerically where the matrix \check{A} is truncated at some finite size N . We will use a small parameter $Z_1 < 1$ to demonstrate the underlying physical processes in the system. Let us first look at the transmission through the system when the static part of the potential is turned off, shown in Fig. 4.2 (a) as in Reference [107]. At low energies $E < \hbar\Omega$

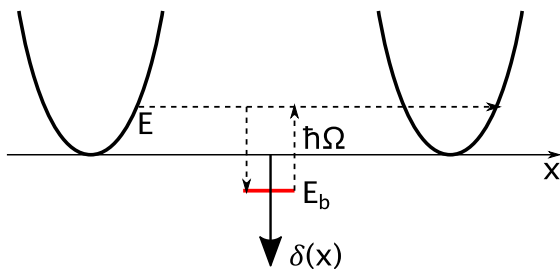


Figure 4.3: The destructive interference between the elastic and the inelastic channels results in the Fano resonance if the quasibound state E_b in the delta-potential well is excited.

only the positive sidebands $n \geq 0$, the negative channels are closed due to imaginary wave vector. The total transmission $T = \sum_n T_n$ is very close to unity since the particle is essentially propagating free, with small effects due to spread to positive sideband channels. However, when the energy reaches $\hbar\Omega$ a new channel $n = -1$ opens up, thus we see a resonance in the transmission. The total transmission has a resonant dip since there is also backscattering in the channel. Exactly at $E = \hbar\Omega$ the wave vector k_{n-1} vanishes resulting in perfect reflection in the main energy channel. After we turn on the static potential well, see Fig. 4.2 (b), the picture changes dramatically. As we know from Chapter 3, a delta potential well hosts a bound state. As the particle scatters from the dynamic barrier it can now access the bound state via emitting and then reabsorbing an energy quantum. Since the bound state is located at negative energy, the resonance happens at a lower energy than without the static well, $E_{-1} = E_b < 0$. Now this state is of course quasibound, since the particle can escape from it, see Fig. 4.3. The resonance profile is highly asymmetric, with a sharp dip followed by a peak, and is generally referred to as a Fano resonance. Ugo Fano described it in 1935 when modelling inelastic scattering of electrons from helium [108, 109]. The spectral shape of a normalized Fano resonance,

$$f(\epsilon) = \frac{(\epsilon + q)^2}{(\epsilon^2 + 1)(q^2 + 1)}, \quad (4.20)$$

is parametrized by two variables: $\epsilon = (E - E_R)/\Gamma$ is the distance from the resonance position E_R adjusted by its broadening Γ and the asymmetry factor q . The asymmetry is roughly described by the ratio between

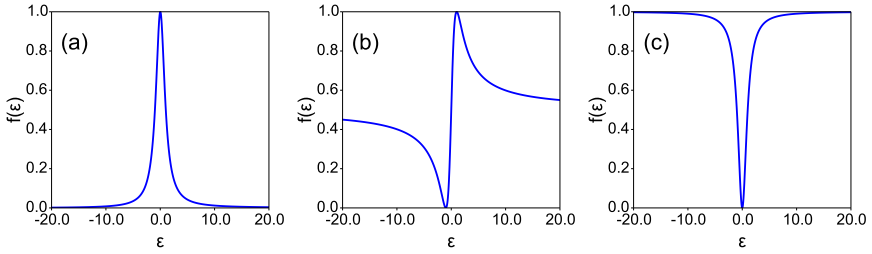


Figure 4.4: Fano resonances at different asymmetry ratios, $\Gamma = 0.05$, (a) $q = 100$ is a Lorentzian peak, (b) $q = 1$ is the perfect symmetry between the peak and the dip, (c) $q = 0$ is a Lorentzian antiresonance.

transmission for the resonant and continuum channels [110]. Setting the asymmetry to infinity results in the resonant channel dominating the picture, producing a symmetric Breit-Wigner resonance (Lorentzian profile), see Fig. 4.4. In the opposite case, $q = 0$, we observe a symmetric dip, an antiresonance, describing non-resonant transmission. Anything in between shares features of both, with q shifting the relative weight between the peaks and dips contribution. Since in our case the quasibound state is an additional feature present on top of the static potential landscape, the resulting resonance can only approximately be described by Fano profile. This discussion is at the phenomenological level, rather than quantitative.

Fano resonance has a classical analogy as two coupled harmonic oscillators, while one is driven by an oscillating force [111]. In this analogy, the propagating mode is one oscillator, coupled to the external drive, while the quasibound state is the other. Zero transmission in our case corresponds to when the motion of the first harmonic oscillator is quenched in the classical case. Since the phenomenon requires only a localized state interfering with a continuum of modes, it appears in many different physical systems, e.g. connected nanotubes [112], quantum dots [113], plasmonics [114]. Resonant behaviour allows for potential applications such as spin filtering [115], sensors [116, 117], and photonic metamaterials [118].

4.3 Floquet theory in graphene

Tien-Gordon theory is of course just a subset of a more general Floquet theory treating time-periodic differential equations [119, 120] of the form

$f'(t) = A(t)f(t)$. It states that if matrix $A(t)$ is periodic, then the solution vector $x(t)$ must not be periodic, but of the form $e^{\alpha t}g(t)$, where $g(t)$ is periodic with the same period as the matrix. From the Tien-Gordon theory one can anticipate that parameter α would be proportional to quasienergy in our case, and the periodic function $g(t)$ is the sideband expansion. One can draw an analogy between Floquet states in our time-dependent problem and Bloch waves in an infinite crystal. Again, the periodicity in the system, lattice in this case, enforces periodicity in the wave function eigenstates. However, unlike crystal structures, which are limited and governed by the chemical composition of materials, the periodic oscillations induced by an external source provide an effective control parameter over a system. Recently a whole field of the so-called Floquet engineering have emerged, with examples like controlling spin-orbit coupling in graphene [121], inducing superconductivity in semiconductors [122], or controlling matter waves [123]. For a deeper discussion on limitations and applicability of Floquet theory please refer to [124] and [125]. For the discussion that follows we simply apply a procedure analogous to what we have done for one-dimensional potential in Schrödinger equation to graphene. Knowing from the Chapter 3 the mapping between graphene and 2DEG, one can extrapolate and write down the boundary condition for the square barrier directly as

$$\begin{cases} \delta_{n0} \begin{pmatrix} 1 \\ \eta_n \end{pmatrix} + r_n \begin{pmatrix} 1 \\ \bar{\eta}_n \end{pmatrix} = \sum_{l=-\infty}^{\infty} \left[b_l \begin{pmatrix} 1 \\ \mu_l \end{pmatrix} + c_l \begin{pmatrix} 1 \\ \bar{\mu}_l \end{pmatrix} \right] J_{n-l} \left(\frac{U_1}{\hbar\Omega} \right) \\ t_n \begin{pmatrix} 1 \\ \eta_n \end{pmatrix} = \sum_{l=-\infty}^{\infty} \left[b_l \begin{pmatrix} 1 \\ \mu_l \end{pmatrix} e^{iq_l D} + c_l \begin{pmatrix} 1 \\ \bar{\mu}_l \end{pmatrix} e^{-iq_l D} \right] J_{n-l} \left(\frac{U_1}{\hbar\Omega} \right), \end{cases} \quad (4.21)$$

where spinor components $\eta_n = \frac{k_n + ik_y}{E_n}$, $\mu_n = \frac{q_n + ik_y}{(E_n - U_0)}$ are defined for all sidebands, and $k_n = \text{sgn}(E_n) \sqrt{E_n^2 - k_y^2}$, $q_n = \text{sgn}(E_n - U_0) \sqrt{(E_n - U_0)^2 - k_y^2}$. Scattering in two dimensions is complicated by the presence of k_y . Here we require it to be conserved, thus waves in different sideband channels scatter at different angles, see Fig. 4.5.

Again, there is a clear difference from the case of non-relativistic particles in the form of possible Klein tunnelling even for time-dependent case. This time, different Dirac cone sections result from a time-dependent drive, see Fig. 4.6. In Papers I-IV, however, we are using a delta-function approximation of the top gate barrier, thus we will derive the boundary condition

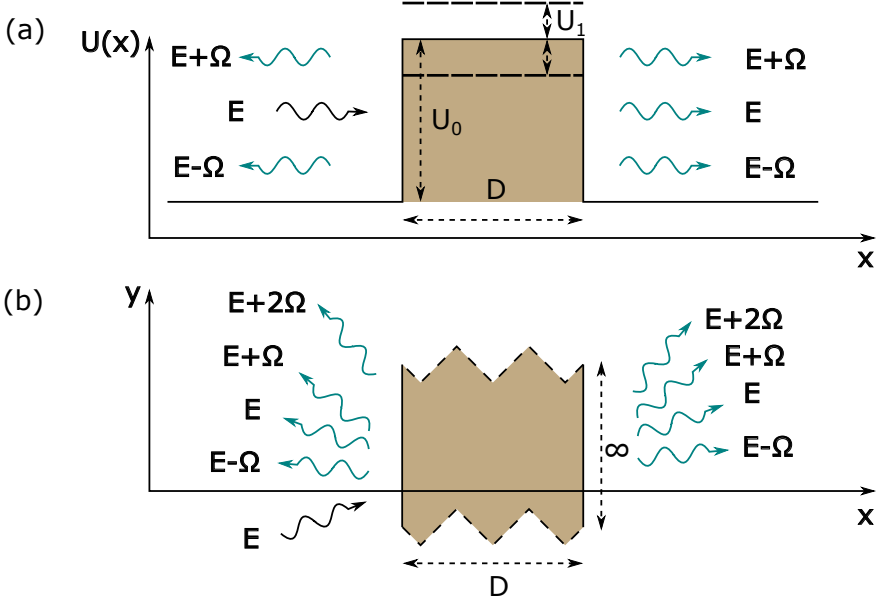


Figure 4.5: Scattering from an oscillating barrier in graphene. (a) Side view of the potential landscape, the oscillating part U_1 causes energy sidebands to form. (b) Top view of the barrier, waves at different sidebands scatter at different angles.

here, starting with the Hamiltonian

$$H(x,t) = -i\hbar v_F \nabla \cdot \boldsymbol{\sigma} + [Z_0 + Z_1 \cos(\Omega t)]\delta(x) \quad (4.22)$$

Setting constants $\hbar = 1$ and $v_F = 1$ and taking the Fourier transform of the corresponding Dirac equations, as in App. B.3, leaves

$$E\Psi(x,k_y,t) = [-i\nabla \cdot \boldsymbol{\sigma} + Z_0\delta(x)]\Psi(x,k_y,E) + \frac{Z_1}{2}\delta(x)[\Psi(x,k_y,E + \Omega) + \Psi(x,k_y,E - \Omega)]. \quad (4.23)$$

Using the short notation $\Psi(x,k_y,E + n\Omega) = \psi_n(x)$, we can write

$$E\psi_n(x) = [-i(\nabla_x \sigma_x) + k_y \sigma_y + Z_0\delta(x)]\psi_n(x) + \frac{Z_1}{2}\delta(x)[\psi_{n+1}(x) + \psi_{n-1}(x)] \quad (4.24)$$

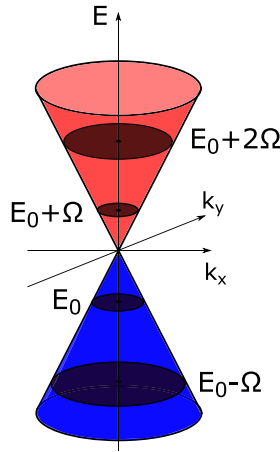


Figure 4.6: Oscillation-induced Dirac cone sections.

By arranging the wave function amplitudes into a vector $\Phi(x)$ in sideband space we arrive at equations (4,5) of Paper I. The boundary condition for graphene therefore is given by

$$\Phi(x = 0^-) = \check{M}\Phi(x = 0^+), \quad (4.25)$$

where $\check{M}_{nm} = \exp[iZ_0\sigma_x](i\sigma_x)^{|n-m|}J_{|n-m|}(Z_1)$ as derived in Paper III. In the connection matrix M we note a familiar factor of $\exp[iZ_0\sigma_x]$, which is the rotation operator in pseudospinor space from the static delta barrier, shown in Chapter 3. It acts on all sidebands. The second factor however comes from the dynamic part of the barrier. Remarkably, Bessel function parameters similar to that of the square well survive in this case, governing coupling between different sidebands. There is a σ_x rotation matrix involved due to the fact that the oscillating potential is also a delta barrier. Note that its power coincides with the sideband index of the Bessel function. Physically we can interpret it as a counter how many times the wave has to scatter off the delta barrier boundaries to pick up $|n - m|$ energy quanta, while each passage involves a rotation by σ_x . The last thing before using the boundary condition derived here is to verify that we are allowed to integrate operators as we have done here.

4.3.1 Magnus expansion of the boundary condition

Let us solve a linear ordinary differential equation with a matrix parameter-dependent coefficient

$$\mathbf{Y}'(t) = \hat{A}(t)\mathbf{Y}(t) \quad (4.26)$$

It is clear that if the operator \hat{A} commutes with itself at all times then we can integrate the operator safely,

$$\forall t_1, t_2 : [\hat{A}(t_1), \hat{A}(t_2)] = 0 \quad \implies \quad \mathbf{Y}(t) = \mathbf{Y}(t_0) \exp\left(\int_{t_0}^t \hat{A}(t_1) dt_1\right). \quad (4.27)$$

Note that square brackets here denote a commutator as $[\hat{a}, \hat{c}] = \hat{a}\hat{c} - \hat{c}\hat{a}$. However, if it does not commute, we can introduce an ansatz

$$\mathbf{Y}(t) = \mathbf{Y}(t_0) \exp(\hat{B}(t, t_0)), \quad (4.28)$$

which after plugging in to the differential equation yields

$$\left(\frac{d}{dt} e^{\hat{B}(t, t_0)}\right) e^{-\hat{B}(t, t_0)} = \hat{A}(t) \quad (4.29)$$

Expanding the coefficient in the Magnus series $\hat{B}(t, t_0) = \sum_k \hat{B}_k(t, t_0)$, we can solve the equation recursively, with the first two coefficients given by

$$\hat{B}_1(t, t_0) = \int_{t_0}^t \hat{A}(t_1) dt_1 \quad (4.30)$$

$$\hat{B}_2(t, t_0) = \frac{1}{2} \int_{t_0}^t dt_1 \int_{t_0}^{t_1} dt_2 [\hat{A}(t_1), \hat{A}(t_2)] \quad (4.31)$$

Subsequent terms contain nested commutators of an increasing complexity. In our case we attempt to solve an equation of the form:

$$\nabla_x \Phi(x) = \tilde{M}(x) \Phi(x), \quad (4.32)$$

where $\tilde{M}_{nm}(x) = (i(E_n - Z_0 \delta(x)) \hat{\sigma}_x - k_y \hat{\sigma}_z) \delta_{nm} - i \frac{Z_1}{2} \delta(x) \hat{\sigma}_x \delta_{|n-m|, 1}$. Clearly the coordinate dependence in the form of $\delta(x)$ separates from the operator (matrix) dependence, while the latter is the source of non-commutativity

due to Pauli matrices. All the constant terms and terms with identical Pauli indices vanish under commutation, leaving us with:

$$\left[\tilde{M}(x_1), \tilde{M}(x_2)\right] = \hat{\alpha}(\delta(x_1) - \delta(x_2)), \quad (4.33)$$

where $\hat{\alpha}$ is the coordinate-independent result of the matrix commutation. The resulting difference between two delta-functions vanishes upon double integration:

$$\begin{aligned} \hat{B}_2(0^+, 0^-) &= \frac{\hat{\alpha}}{2} \int_{0^-}^{0^+} dx_1 \int_{0^-}^{x_1} dx_2 (\delta(x_1) - \delta(x_2)) = \\ &= \frac{\hat{\alpha}}{2} \int_{0^-}^{0^+} dx_1 (x_1 \delta(x_1) - \theta(x_1)) = \\ &= 0 \end{aligned} \quad (4.34)$$

Thus the commutator prefactor in the Magnus expansion always gives zero under integration, and all higher-order terms $B_{n>2}$ vanish, leaving us with the standard result for commuting matrices B_1 . Here we should note that the result is trivially true under the assumption that the delta barrier is the correct limit of the square barrier with vanishingly small width and proportionally infinite height.

Chapter 5

Transport theory

In this chapter we follow a well-established Landauer-Büttiker scattering theory [28, 126, 127] for electronic transport. Within this formulation, we relate the experimental observables like electron current and noise to tunnelling amplitudes discussed in previous chapters. We show the derivation of the observables for the time-independent case and later generalise it to the oscillating potential scenario.

5.1 Electron current in second quantization

5.1.1 Historical perspective

Development of nanotechnology has put challenges in front of physics community in the description of electronic transport. As the dimensions of transistors got smaller, the laws of classical physics could no longer describe the results of measurements. There are three length scales involved in the problem in addition to the geometry of the device (W): the mean free path of electrons l_e describing the collisions between particles, the Fermi wavelength λ_F derived corresponding to the kinetic energy of the charge carriers, and the phase coherence length after which information about initial quantum state is lost. The macroscopic conductor's size is typically larger than any of these scales and thus classical behaviour is observed. We also know that on microscopic (atomic) scale, quantum effects dominate the picture. For W on the order of $10\text{ nm} - 1\text{ }\mu\text{m}$ we fall exactly in between these two, this area is called mesoscopic physics. The Fermi wavelength

is important for conduction especially at low temperatures since most of the excitations are close to the Fermi level, and contributions to transport properties of those far away from it can be neglected. The mean free path of electrons determines when the original momentum of the particle is lost. This thesis is focused on ballistic devices, meaning that l_e is larger than geometric dimensions and electrons fly through it without collisions. The phase relaxation length is usually dominated by scattering off active impurities and electron-electron interaction at low temperatures. The latter be low due to the small density of states available for excitations around the Fermi level and the phase coherence time is on the order of momentum relaxation time for high mobility semiconductors [128].

Research into mesoscopic physics has been boosted after development of 2DEG which allowed to nanoscale-sized transistors with large electron mobility. Rolf Landauer in 1957 has suggested that the conductance of a mesoscopic system is related rather to the transmission probability through it rather than just applied electric field [129]. The well-known relation of a 2D metallic conductor to its length L and width W

$$G = \sigma W/L, \quad (5.1)$$

where σ is its conductivity and is independent of geometrical dimensions, postulates that the conductance is simply proportional to the width of the conducting channel. However, studies of point contacts in 2DEGs revealed that it is no longer the case, see Fig. 5.1 when the width is sufficiently narrow [130] with the dependence becoming discrete confirming prediction of Landauer. The formula proposed by him has the form

$$G = \frac{2e^2}{h} NT, \quad (5.2)$$

where N is the number of transverse channels in the conductor arising due to quantum confinement and T is the average transmission probability for them. Together with Büttiker, Landauer refined and generalized the theory to a multi-terminal and time-dependent case [28, 126, 127, 131]. Below we will reproduce some of the key steps of this crucial derivation for 2DEG and later on highlight differences to graphene.

5.1.2 Transverse modes

So how do transverse channels come about in (5.2)? Let us imagine a toy system of a quantum point contact, shown in Fig. 5.1. It can be

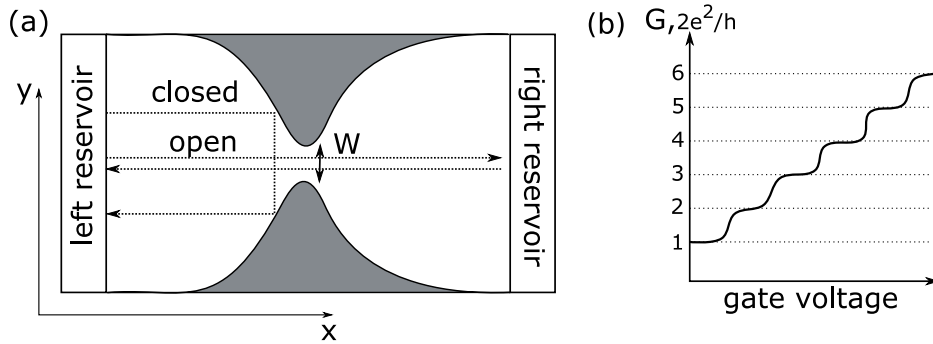


Figure 5.1: Quantum point contact. (a) Constriction of a waveguide by gate voltage leads to some channels being closed, that results in (b) quantization of conductance of the sample, following the experiment in [130].

modelled as an adiabatic waveguide with a narrow constriction of width W . In the original experiment of Ref. [130] the confinement is achieved by applying a repulsive gate potential. It is adiabatic in a sense that the left and right reservoirs are much larger and smoothly connect to the constriction in the middle on a large scale, so that locally we can view it as an ideal parallel waveguide. We can then solve Schrödinger equation by separation of variables, yielding the wave function to have the form $\Psi(x, y, t) = \psi_x(x)\psi_y(y)e^{iEt/\hbar}$. The transverse component can be obtained from the boundary condition requiring the wave function to vanish at the edges of the waveguide. Assuming it has the form $\psi_y(y) = Ae^{ik_y y} + Be^{-ik_y y}$ one finds that $B = -A$ and the allowed values of transverse momentum are quantized as

$$k_y^n = \frac{n\pi}{W}, \quad (5.3)$$

where the index of transverse channels $n < N$ has a cutoff $N = \text{int}(2W/\lambda_F)$. Given that the dispersion relation, now we get a channel-dependent energy $E_n = \frac{\hbar^2}{2m} \left(k_x^2 + \left(\frac{n\pi}{W} \right)^2 \right)$, we get a different number of open quantum channels in the wide section of the conductor and in the constriction. Including normalization, each transverse mode is given by

$$\psi_y^n(y) = \sqrt{\frac{2}{W}} \sin \left(\frac{n\pi}{W} y \right) \quad (5.4)$$

Now the transmission of each individual channel is unity here. However, if we incorporate a tunnel barrier described in Chapter 3 into the constriction,

we obtain a channel-dependent transmission. We know that very far to the left and right we have propagating waves in the longitudinal direction, and we can use boundary condition matching to determine the transmission properties of the barrier.

5.1.3 Scattering basis

In the absence of transverse confinement we can say that the most general solution to the Schrödinger equation is given by

$$\Psi(x,y,t) = \frac{1}{2\pi} \iint dk_x dk_y a(k_x, k_y) e^{ik_x x} e^{ik_y y} e^{-iEt/\hbar} \quad (5.5)$$

in stationary case with amplitude $a(k_x, k_y)$. We note that that each integral in momentum space brings a factor $1/\sqrt{2\pi}$. The case is generalized trivially to three dimensions. Since energy E and transverse momentum k_y are good quantum numbers, using the dispersion relation we can rewrite the longitudinal momentum as $k_x = \pm k = \pm\sqrt{2mE/\hbar^2 - k_y^2}$ and separate the states into "right-movers" ($k_x = k > 0$) and "left-movers" ($k_x = -k < 0$) so that

$$\int_{-\infty}^{\infty} dk_x \Psi(k_x, k_y, t) = \int_0^{\infty} d(-k) \Psi(-k, k_y, t) + \int_0^{\infty} dk \Psi(k, k_y, t). \quad (5.6)$$

We call waves propagating with wave vector k right-movers since their group velocity along x-axis $v = \frac{1}{\hbar} \frac{\partial E}{\partial k_x} = \frac{\hbar k}{m}$ is positive, thus they propagate to the right. We can also transform the momentum integral into the energy integral using

$$dk = \frac{1}{\sqrt{\frac{2mE}{\hbar^2} - k_y^2}} \frac{m}{\hbar^2} dE = \frac{1}{\hbar v} dE, \quad (5.7)$$

thus bringing the wave function into the form

$$\Psi(x,y,t) = \int \frac{dk_y}{2\pi} \int_{\frac{\hbar^2 k_y^2}{2m}}^{\infty} dE \left(\frac{a(k, k_y)}{\hbar v} e^{ikx} + \frac{a(-k, k_y)}{\hbar v} e^{-ikx} \right) e^{ik_y y} e^{-iEt/\hbar}$$

Introducing the amplitudes for left- and right-movers in energy representation as

$$a(E, k_y) = \frac{1}{\sqrt{\hbar v(E, k_y)}} a(k, k_y) \quad (5.8)$$

$$b(E, k_y) = \frac{1}{\sqrt{\hbar v(E, k_y)}} a(-k, k_y), \quad (5.9)$$

we obtain the expression for the wave function in terms of them. For transverse confinement the same procedure can be repeated keeping in mind that the transverse modes are now quantized, giving

$$\Psi(x, y, t) = \int_0^\infty dE e^{-iEt/\hbar} \sum_{n=1}^{N(E)} \frac{\psi_y^n(y)}{\sqrt{2\pi\hbar v_n(E)}} \left(a_n(E) e^{ik_n x} + b_n(E) e^{-ik_n x} \right), \quad (5.10)$$

where $v_n(E) = \frac{\hbar}{m} k_n(E)$ and $k_n(E) = \frac{1}{\hbar} \sqrt{2m(E - E_y^n)}$, $E_y^n = \frac{\hbar^2 \pi^2}{2mW^2} n^2$. Thus for every channel we have corresponding incoming a_n (right-moving) and outgoing b_n (left-moving) amplitudes. This scattering basis (transverse wave functions are orthonormal) is basically the starting point of Büttiker theory [28].

5.1.4 Field operators in second quantization

So far we have been treating it in a single-particle approach. In reality a mesoscopic conductor contains a huge number of electrons, thus requiring to solve a many-body Schrödinger equation with too many degrees of freedom, making the exact solution computationally unfeasible. Instead we consider quasiparticle excitations of the ground state of the system. Since we are dealing with fermions, Pauli exclusion principle prevents them from occupying the same state and we end up with all individual particle states filled up to the Fermi level. If the perturbations applied to the system, e.g. voltage and temperature fluctuations, are small enough, all quasiparticles are located within the vicinity of the Fermi level in the energy range $\Delta E \sim \max(k_B T, U)$. The density of states in this energy window is smaller than that of electrons in the metal and allows to neglect interactions between the excitations, for example the electric field around quasiparticle excitations gets screened by the ground state electrons thus reducing long-range Coulomb interaction. The quasiparticle spin, charge

and momentum are the same as the original non-interacting particles, while their mass gets renormalised due to interactions. This proposed by Lev Landau model earned him the Nobel prize in 1962. To keep track of our quasiparticle excitations we will treat them in the second quantization, meaning that all amplitudes we discussed before become operators acting on a Fock state basis

$$\Psi(x,y,t) \rightarrow \hat{\Psi}(x,y,t) \quad (5.11)$$

$$\Psi^*(x,y,t) \rightarrow \hat{\Psi}^\dagger(x,y,t) \quad (5.12)$$

A field operator $\hat{\Psi}(x,y,t)$ annihilates a particle at spacetime coordinate (x,y,t) , and together with the creation operator $\hat{\Psi}^\dagger(x,y,t)$ they satisfy commutation relations

$$\{\hat{\Psi}(x,y,t), \hat{\Psi}^\dagger(x',y',t)\} = \delta(x-x')\delta(y-y') \quad (5.13)$$

$$\{\hat{\Psi}(x,y,t), \hat{\Psi}(x',y',t)\} = \{\hat{\Psi}^\dagger(x,y,t), \hat{\Psi}^\dagger(x',y',t)\} = 0 \quad (5.14)$$

Amplitudes $a_n(E)$ become annihilation operators for particles in respective transverse channels, defined via

$$\hat{a}_n(k,t) = \frac{1}{\sqrt{2\pi}} \iint dx dy e^{-ikx} \psi_y^n(y) \hat{\Psi}(x,y,t) = \hat{a}_n(k) e^{-iE_n(k)t}, \quad (5.15)$$

where E_n is the energy of the n^{th} transverse channel. One can verify, see App. D that they satisfy the corresponding commutation relations

$$\{\hat{a}_n(k), \hat{a}_m^\dagger(k')\} = \delta_{nm} \delta(k-k') \quad \text{and} \quad (5.16)$$

$$\{\hat{a}_n(E), \hat{a}_m^\dagger(E')\} = \delta_{nm} \delta(E-E'). \quad (5.17)$$

The probability current operator can be derived from the continuity equation

$$\frac{\partial}{\partial t} |\hat{\Psi}(x,y,t)|^2 + \nabla \hat{\mathbf{j}} = 0, \quad (5.18)$$

and Heisenberg operator time evolution $i\hbar \frac{\partial}{\partial t} \hat{O} = [\hat{O}, \hat{H}]$, giving

$$\hat{j}(x,y,t) = \frac{i\hbar}{2m} \left(\hat{\Psi}(x,y,t) \nabla \hat{\Psi}(x,y,t)^\dagger - \hat{\Psi}(x,y,t)^\dagger \nabla \hat{\Psi}(x,y,t) \right), \quad (5.19)$$

which of course has the same form as the textbook non-operator equivalent. The total electrical current operator is the integral over it in the transverse direction

$$\hat{I}_\alpha = e \int_0^W dy j_\alpha(x,y,t), \quad (5.20)$$

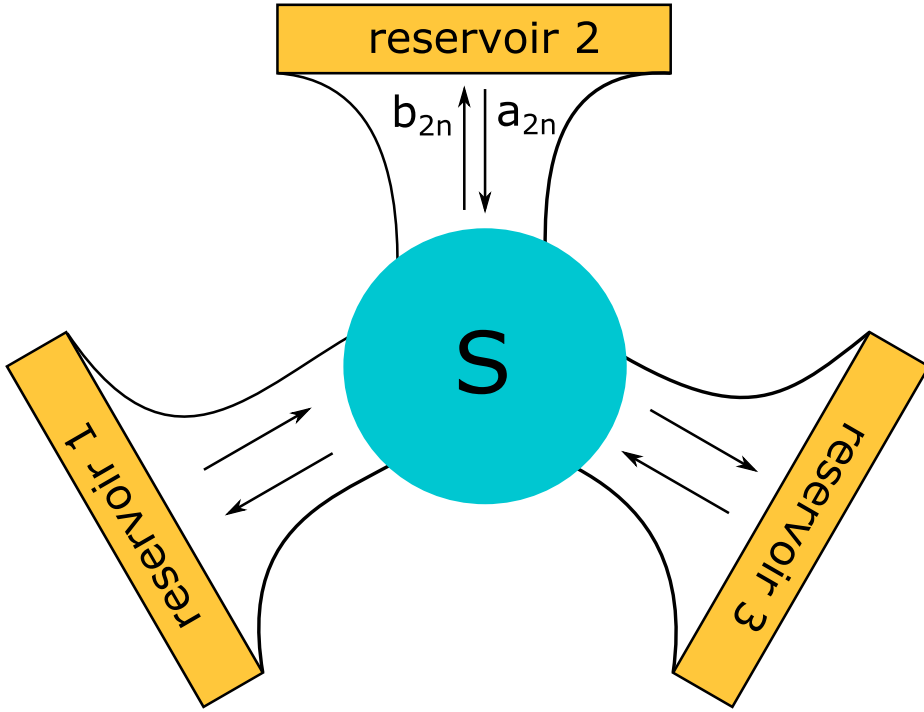


Figure 5.2: Multi-terminal scattering can be described by a scattering matrix S connecting waves b outgoing from the scattering region into one terminal with incoming a from all other reservoirs.

where e is the electron charge. Here we introduce an electrode index α where the current is measured with respect to waves incident from the left reservoir.

5.1.5 Scattering matrix

One has to realise that the scattering amplitudes a and b can be related via a scattering matrix

$$\hat{b}_{n\alpha}(E) = \sum_{m,\beta} S_{\alpha\beta,nm}(E) \hat{a}_{m\beta}(E), \quad (5.21)$$

$$\hat{b}_{n\alpha}^\dagger(E) = \sum_{m,\beta} [S_{\alpha\beta,nm}(E)]^\dagger \hat{a}_{m\beta}^\dagger(E), \quad (5.22)$$

where α, β are reservoir indices and n, m are channel indices. By this definition $S_{\alpha\beta, nm}$ relates an outgoing wave in reservoir α and transverse channel n with an incoming one from reservoir β and channel m . We define it in such a way that the operators \hat{a} and \hat{b} are normalized to unit probability flux. Coming back to our picture of a QPC, the reservoirs are connected via ideal waveguides to the constriction, which we will call the scattering region from now on, see Fig. 5.2. The ingenuity of the method relies on the fact that we view the scattering region as a black box, with some complicated scattering going on within it, but what we care about are the plane waves propagating in the waveguides towards the reservoirs. Thus the scattering matrix is defined only for plane waves. Given the reflection and transmission coefficients obtained from solving the boundary condition problem within the scattering region, we can write the scattering matrix as

$$S = \begin{pmatrix} S_{LL} & S_{LR} \\ S_{RL} & S_{RR} \end{pmatrix} = \begin{pmatrix} r & t' \\ t & r' \end{pmatrix}, \quad (5.23)$$

and is related to the transmission and reflection coefficients that we have been deriving in the previous chapters. For example r here represents an $N_L \times N_L$ reflection matrix describing the waves incoming from the left that get reflected back into the left reservoir, where N_L is the number of open channels on the left, while primed quantities describe scattering if the incident wave is from the right. The scattering matrix thus provides us with the complete information about the scattering region, while operators $\hat{a}_{n\alpha}^\dagger$ create propagating particles in the specified reservoir and channel that will impede onto the scattering region, they contain only information about the local reservoir environment. The formula is in principle applicable to a multi-terminal setup, while in this work we will use the simplest setup with two reservoirs, left (L) and right (R) corresponding to the source and drain in a transistor. The scattering matrix possesses a few key properties. Since the particle number is conserved during scattering, it has to be unitary

$$S^\dagger S = S S^\dagger = \hat{I}. \quad (5.24)$$

Under micro-reversibility if we change time $t \rightarrow -t$ and velocity $v \rightarrow -v$, the particle will move in the opposite direction. We did not introduce any magnetic field or other process breaking the time-reversal symmetry, thus the physics stays the same. However, from the point of view of the scattering matrix, the incoming and outgoing states change places. This

requires

$$S^\dagger = S^{-1} \quad (5.25)$$

$$S_{\alpha\beta, mn} = S_{\beta\alpha, nm} \quad (5.26)$$

In this notation the transmission probabilities are written as $T(E) = \text{Tr}[\hat{t}^\dagger \hat{t}]$. Also note that the unitary requirement from the scattering matrix gives us $\text{Tr}[S^\dagger S] = R(E) + T(E) = 1$, an intuitive result stating the probability conservation.

Returning to our current operator, plugging in the scattering operators, we obtain

$$\begin{aligned} \hat{I}_L &= \frac{e\hbar}{2mi} \int_0^W dy \sum_{n,m} \int_{E_y^n}^\infty dE \int_{E_y^m}^\infty dE' e^{i(E-E')t/\hbar} \frac{\psi_y^n(y)\psi_y^m(y)}{2\pi\hbar\sqrt{v'_n v'_m}} \\ &\times \left\{ \left[\hat{a}_{nL}^\dagger e^{-ik_n x} + \hat{b}_{nL}^\dagger e^{ik_n x} \right] \left[ik_m \hat{a}'_{mL} e^{ik_m x} - ik_m \hat{b}'_{mL} e^{-ik_m x} \right] \right. \\ &\left. - \left[ik_n \hat{a}_{nL}^\dagger e^{-ik_n x} + ik_n \hat{b}_{nL}^\dagger e^{ik_n x} \right] \left[\hat{a}'_{mL} e^{ik_m x} + \hat{b}'_{mL} e^{-ik_m x} \right] \right\}, \quad (5.27) \end{aligned}$$

where we have omitted explicit energy dependence $v = v(E)$ and $v' = v(E')$. Taking the products of operators and using orthonormality of the transverse components, we can write

$$\begin{aligned} \hat{I}_L &= \frac{e}{4\pi\hbar} \sum_n \int_{E_y^n}^\infty dE \int_{E_y^n}^\infty dE' \frac{e^{i(E-E')t/\hbar}}{\sqrt{v'_n v'_n}} \\ &\times \left\{ [v_n + v'_n] \left[\hat{a}_{nL}^\dagger \hat{a}'_{nL} e^{-i(k_n - k'_n)x} - \hat{b}_{nL}^\dagger \hat{b}'_{nL} e^{i(k_n - k'_n)x} \right] \right. \\ &\left. + [v_n - v'_n] \left[\hat{a}_{nL}^\dagger \hat{b}'_{nL} e^{-i(k_n + k'_n)x} - \hat{b}_{nL}^\dagger \hat{a}'_{nL} e^{i(k_n + k'_n)x} \right] \right\}, \quad (5.28) \end{aligned}$$

which corresponds to expression (31) in the review article by Büttiker and Blanter [132]. Now the original argument by them goes as following: all observables like average current, noise, etc. are in the energy window around the Fermi level for which energies E and E' are close to each, while the velocities $v(E)$ vary slowly, typically on the scale of Fermi energy. Then we can assume them to be identical $v(E', k_y) \approx v(E, k_y)$, while the exponential factors $e^{i(k_n - k'_n)x}$ reduce to unity (the oscillations are too fast due to large momentum k_n). We note that this assumption is not always true in relation to charge carriers in graphene, for which quasimomentum k

is small in the vicinity of Dirac point. Nevertheless, under this assumption for 2DEG, the last formula simplifies considerably to

$$\hat{I}_L = \frac{e\hbar}{2\pi\hbar} \sum_n \int_{E_y^n}^{\infty} dE \int_{E_y^n}^{\infty} dE' e^{i(E-E')t/\hbar} [\hat{a}_{nL}^\dagger \hat{a}'_{nL} - \hat{b}_{nL}^\dagger \hat{b}'_{nL}]. \quad (5.29)$$

Finally, introducing the relation between the incoming and outgoing states via the scattering matrix we obtain

$$\begin{aligned} \hat{I}_L &= \frac{e\hbar}{2\pi\hbar} \sum_n \iint_{E_y^n}^{\infty} dE dE' e^{i(E-E')t/\hbar} [\hat{a}_{nL}^\dagger \hat{a}'_{nL} \\ &\quad - \sum_{\alpha,\beta} \sum_m \sum_{m'} [S_{L\alpha,nm}]^\dagger S_{L\beta,nm'} \hat{a}_{m\alpha}^\dagger \hat{a}'_{m'\beta}]. \end{aligned} \quad (5.30)$$

Now we are left with the final step: to obtain the value of current we have to calculate its statistical average.

5.1.6 Statistical averages

We assume electron relaxation to happen in reservoirs, once a particle is scattered into it, it equilibrates with the thermal bath and never comes back to the scattering region. The reservoirs are kept in local equilibrium at respective chemical potential μ_α and temperature Ξ_α . Based on the grand canonical ensemble in the occupation number representation one can derive the operator averages in one reservoir to be

$$\langle \hat{a}_n^\dagger(k_x) \hat{a}_m(k'_x) \rangle = \delta(k_x - k'_x) \delta_{nm} \frac{1}{1 + \exp[E_n(k_x) - \mu]/k_B \Xi}, \quad (5.31)$$

where the last fraction is nothing else but the Fermi distribution $f(E)$. The formula is then readily generalized to multiple contacts in energy representation

$$\langle \hat{a}_{\alpha n}^\dagger(E) \hat{a}_{\beta m}(E') \rangle = \delta_{\alpha\beta} \delta_{nm} \delta(E - E') f_\alpha(E). \quad (5.32)$$

Plugging it into the expectation value for current we get

$$\langle I_L \rangle = \frac{e}{2\pi\hbar} \sum_n \int_{E_y^n}^{\infty} dE \left\{ f_\alpha(E) - \sum_\beta \sum_m [S_{L\beta,nm}(E)]^\dagger S_{L\beta,nm}(E) f_\beta(E) \right\} \quad (5.33)$$

which after using unitarity of the scattering matrix can be rewritten as

$$\langle I_L \rangle = \frac{e}{2\pi\hbar} \sum_n \int_{E_y^n}^{\infty} dE \sum_{\beta} \sum_m [S_{L\beta,nm}(E)]^\dagger S_{L\beta,nm}(E) [f_L(E) - f_\beta(E)] \quad (5.34)$$

First we should note that the scattering matrices have the same indices, which means the corresponding value is positive real. Notice the difference between the Fermi distributions in the reservoirs. It makes physical sense since setting $\alpha = \beta$ directly yields zero, otherwise the particles can come from one reservoir to another only if there are unoccupied states available due to Pauli exclusion principle.

If we apply a small external source-drain bias eV_{LR} to the identical leads at the same temperature, we modify the chemical potential, say in the source, as $\mu_L = \mu - eV_{LR}$. We can then write down the current relating it to the conductance matrix $G_{\alpha\beta}$ and the applied voltage as

$$\langle I_\alpha \rangle = \sum_{\beta} G_{\alpha\beta} V_{\alpha\beta}. \quad (5.35)$$

The Fermi functions at zero temperature are reduced to step functions around the chemical potential, while the difference between them reduces to a delta function in the energy space around the Fermi energy E_F , which collapses the energy integral, see App. E, giving us the expression for linear conductance

$$G_{LR} = \frac{e^2}{2\pi\hbar} \text{Tr}[t^\dagger(E_F)t(E_F)]. \quad (5.36)$$

Here we reiterate that the scattering matrices are defined for open channels, thus the limits in the sums and integration above have to ensure that, specifically defining the band bottom in corresponding energy channels $E_F > E_y^n$ and the total number of open channels $m < N_\beta(E_F)$. Now after developing the whole theory, we note that the last expression is nothing else but the suggestion of Landauer that we started our discussion in this chapter with. For identical transverse channels the trace of transmission matrix is just the number of channels time the transmission probability of a single channel. But it turns out the framework described here is much more powerful and can be applied to a broader range of systems.

5.2 Floquet scattering matrix

In Chapter 4 we considered a time-periodic Hamiltonian and described Floquet eigenstates of it. Here we will generalise the scattering matrix formalism to such systems. There is a number of papers describing mesoscopic theory in such systems [133, 134] including Büttiker's works with co-authors [135–137]. It turns out that we can define a so-called Floquet scattering matrix for time-periodic potential perturbations, which takes into account formation of sidebands around the quasienergy E . While much of Büttiker's work concentrated on describing transport under the time-dependent source-drain bias, which in the end is related to the Tien-Gordon effect, in our work we describe scattering from an oscillating potential, so we will concentrate on a latter case here. We consider a very wide channel for simplicity, thus instead of transverse modes we look at a continuum of channels k_y , and the quantization comes from the energy sidebands instead. The relation between the incoming and outgoing particles is then given by

$$\hat{b}_\alpha(E, k_y) = \sum_\beta \sum_{l, E_l \geq E_y} S_{\alpha\beta}(E, E_l; k_y) \hat{a}_\beta(E_l, k_y), \quad (5.37)$$

with corresponding hermitian conjugate creation operator, where l is the sideband index in energy space and $E_l \geq E_y$ ensures that we consider propagating modes only, we will omit writing this restriction explicitly hereon. Thus the sum now has to run over sideband indices to include all possible scattering processes described in Chapter 4, with $S_{\alpha\beta}(E, E_l; k_y)$ describing a particle outgoing at energy E in lead α while the incoming particle had energy $E + l\hbar\Omega$ in lead β . For transverse confinement we get an extra sum over transverse channel index, making the expression a bit more cumbersome. The derivation procedure for current remains the same in all cases. The unitary condition for the scattering matrix becomes

$$\sum_\alpha \sum_n = S_{\alpha\beta}^\dagger(E_n, E_m) S_{\alpha\gamma}(E_n, E) = \delta_{m0} \delta_{\beta\gamma}. \quad (5.38)$$

Since $\cos(\Omega t) = \cos(-\Omega t)$, the Hamiltonian remains invariant under time reversal and micro-reversibility reads $S_{\alpha\beta}(E_n, E) = S_{\beta\alpha}(E, E_n)$. In a completely analogous way to the previous section we can write down the current

operator

$$\begin{aligned}
\hat{I}_\alpha(x,t) &= \frac{e}{2h} \int_{-\infty}^{\infty} \frac{dk_y}{2\pi} \iint_{E_y}^{\infty} dE dE' \frac{e^{i(E-E')t/\hbar}}{\sqrt{v_\alpha v'_\alpha}} \\
&\quad \times \left\{ [v_\alpha + v'_\alpha] \left[e^{-i(k-k')x} \hat{a}_\alpha^\dagger \hat{a}'_\alpha - e^{i(k-k')x} \times \right. \right. \\
&\quad \times \sum_{\gamma\beta} \sum_{l,l'} S_{\alpha\beta}(E, E_l; k_y)^\dagger S_{\alpha\gamma}(E', E'_l; k_y) \hat{a}_{\beta,l}^\dagger \hat{a}'_{\gamma,l'} \left. \right] + \\
&+ [v_\alpha - v'_\alpha] \left[e^{-i(k+k')x} \sum_{\beta} \sum_{l'} S_{\alpha\beta}(E', E'_l; k_y) \hat{a}_\alpha^\dagger \hat{a}'_{\beta} - \right. \\
&\quad \left. \left. - e^{i(k+k')x} \sum_{\beta} \sum_{l'} S_{\alpha\beta}(E, E_l; k_y)^\dagger \hat{a}_{\beta,l}^\dagger \hat{a}'_\alpha \right] \right\} \quad (5.39)
\end{aligned}$$

Here we used short notation, using the explicit energy and momentum dependence $v(E', k_y) = v'$ and $\hat{a}'_{\beta,l} = \hat{a}_\beta(E'_l, k_y)$ everywhere except in scattering matrices. To compute current we need to perform statistical averages of operators

$$\langle \hat{a}_\alpha^\dagger \hat{a}'_\alpha \rangle = \delta(E - E') f_\alpha(E) \quad (5.40)$$

$$\langle \hat{a}_{\beta,l}^\dagger \hat{a}'_{\gamma,l'} \rangle = \delta_{\gamma\beta} \delta(E_l - E'_{l'}) f_\beta(E_l) \quad (5.41)$$

$$\langle \hat{a}_\alpha^\dagger \hat{a}'_{\beta,l'} \rangle = \delta_{\alpha\beta} \delta(E - E'_{l'}) f_\alpha(E) \quad (5.42)$$

$$\langle \hat{a}_{\beta,l}^\dagger \hat{a}'_\alpha \rangle = \delta_{\alpha\beta} \delta(E_l - E') f_\alpha(E_l) \quad (5.43)$$

Plugging it into the current expectation value we get

$$\begin{aligned}
I_\alpha(x,t) &= \frac{e}{h} \int_{-\infty}^{\infty} \frac{dk_y}{2\pi} \int_{E_y}^{\infty} dE \left\{ f_\alpha(E) - \right. \\
&- \sum_{\beta,l,m} \frac{v + v_m}{2\sqrt{vv_m}} e^{-im\Omega t} f_\beta(E_l) S_{\alpha\beta}(E, E_l; k_y)^\dagger S_{\alpha\beta}(E_m, E_l; k_y) e^{i(k-k_m)x} \\
&\quad + \sum_l \frac{v - v_l}{2\sqrt{vv_l}} e^{-il\Omega t} f_\alpha(E) S_{\alpha\alpha}(E_l, E; k_y) e^{-i(k+k_l)x} \\
&\quad \left. - \sum_l \frac{v - v_l}{2\sqrt{vv_l}} e^{-il\Omega t} f_\alpha(E_l) S_{\alpha\alpha}(E, E_l; k_y)^\dagger e^{i(k+k_l)x} \right\} \quad (5.44)
\end{aligned}$$

Here one can verify that current is a real quantity by expanding it in harmonics

$$I_\alpha(x,t) = I_\alpha^0(x,\Omega) + 2\Re \left[\sum_m I_\alpha^m(x,\Omega) e^{-im\Omega t} \right], \quad (5.45)$$

where harmonic amplitudes satisfy $I_\alpha^m = (I_\alpha^{-m})^*$. Again we note that all sums and integrals are performed over propagating states. Büttiker's argument about fast oscillations due to Fermi level can be applied here as well, but one has to be careful now since energy sidebands E_l can extend further from the Fermi surface, so this argument is best applicable only for slow/weak driving.

5.2.1 Scattering formalism in graphene

Since in our papers we discuss time-dependent transport in graphene, it is worth mentioning the key difference in derivation of scattering matrix formalism for it. First of all, since the Hamiltonian has a matrix form in sideband space, its eigenvectors are pseudospinors and we have associate creation/annihilation operator with respective spinors. However, the fermionic commutation relations and Fermi-Dirac distribution requirements in the reservoirs still have to be satisfied. Second, since technically the electron and hole bands touch each, while holes propagate in the opposite direction to electrons, one has to be careful when defining the incoming/outgoing states with respect to the scattering region. The key steps of derivation are presented in Appendix D of Paper I. By comparing (5.44) given here for 2DEG with (D13) in the paper one notices very big similarity, apart from the prefactors due to the linear dispersion of graphene and pseudospinor structure. What is different in graphene is that Büttiker's argument about neglecting fast oscillating terms of the form $e^{i(k-k')x}$ is no longer valid here, and the full expression has to be evaluated. Remarkably, for a static delta barrier and zero contact doping, all extra terms vanish leaving us with differential conductance per unit length given by Landauer formula again,

$$G = \frac{1}{2\pi} \frac{e^2}{h} \int_{-\infty}^{\infty} dk_y T(E_F) = \frac{e^2}{\pi h} E_F \frac{\cos Z_0 - \sin^2 Z_0 \tanh^{-1}(\cos Z_0)}{(\cos Z_0)^3}. \quad (5.46)$$

Here we plugged in the explicit expression for transmission (3.13). It turns out that we can expand the nested trigonometrical functions since $\cos Z_0$ is bounded between -1 and 1, leaving us with a 0.5 percent error approximation if we write the conductance as

$$G \approx \frac{e^2}{\pi h} \left(1 - \frac{|\sin Z_0|}{3}\right). \quad (5.47)$$

Now it is explicit that the periodicity of the delta barrier in terms of the gate strength Z_0 is reflected in static conductance. In the absence of barrier the conductance reaches its maximum value, while backscattering reduces it by a small fraction since the transport is dominated by Klein tunnelling. One final remark here is that the derivation in this chapter did not consider the degeneracy of our quantum channels. For 2DEG there is spin degree of freedom, bring a factor of two to the total current, while for graphene there is an additional factor two coming from K and K' valley energy degeneracy.

5.2.2 Current noise

In Paper III we derive a corresponding operator representation for current noise, which in principle is a current-current correlator at different times, see (A9) in the paper. It describes fluctuations of current around its mean value and its non-vanishing value is a manifestation of quantized nature of electronic charge. The only complication in extending scattering matrix formalism to describe it is that the statistical averages of products of four creation/annihilation operators have to be computed. Noise usually has two fundamental contributions, thermal component and shot noise [134]. The thermal component arises due to random excitations of the Fermi sea due to finite temperature. Even if reservoirs in the system have the same chemical potential, thermal noise still manifests itself. At zero temperature, however, the shot noise remains which is a result of discrete events of particle arrival in electrodes. As a measure of device performance, one can compute the Fano factor, which is an inverse of signal-to-noise ratio,

$$F = \frac{\mathbb{N}}{eG_0}, \quad (5.48)$$

where \mathbb{N} represents a differential shot noise and G_0 the DC differential conductance component. In DC limit, the Fano factor can be presented in terms of transmission probability in individual channels as

$$F = \frac{\sum_n T_n(E_F)[1 - T_n(E_F)]}{\sum_n T_n(E_F)} \quad (5.49)$$

One can notice that in a tunnel barrier $T_n \ll 1$, Fano factor approaches unity. It means that scattering process is actually in Poissonian statistics limit, meaning that arrivals of electrons at an electrode are completely

separate, uncorrelated events. In the opposite limit, the Fano factor approaches zero. Thus the correlations in the system not only display quantized nature of charge but also depend on the nature of particle scattering in the system. One of the reasons to study shot noise in graphene is that there is reduced backscattering in individual channels due to Klein tunnelling, thus the system has high correlation and the noise is low, which is beneficial for device performance. As a final remark here, we refer the reader to the work [138], where the authors show from analytical and numerical simulations in tight-binding model that continuum approximation in the transverse direction that we used in our papers works for a wide enough strip of graphene, showing reasonable results already for $W/L > 4$.

Chapter 6

Paper overview

In this chapter we give a brief description of the main results in the four appended theory papers and relate it to the concepts introduced in the previous chapters of the thesis. I also list my personal contributions to the papers.

6.1 Paper I

In the first paper, we describe quantum transport through a graphene-based transistor with an AC-driven top gate. To do that we have developed a scattering formalism for graphene akin to the existing Landauer-Büttiker theory of mesoscopic transport in 2DEG, as introduced in Chapter 5. Due to the energy sideband generation by the time-dependent drive, see Chapter 4, we use Floquet scattering matrix to derive conductance through the device. As we model the top gate potential as a delta barrier, see Chapter 3, we find that it hosts a bound state which can be accessed both by electron- and hole-like excitations. In the setup of Paper I, we assume that source and drain electrodes introduce no doping, thus scattering amplitudes are all given by the interaction with the delta barrier. Given that only propagating states are allowed to be injected from the source and drain, the bound state interaction is limited to inelastic scattering. Scattering via a quasibound state is shown to produce resonances in the main energy band and second sideband transmission coefficients, which follow Klein tunnelling scenario otherwise. We use second-order perturbation theory in delta barrier strength to derive analytically the shapes of the resonances, confirming that the main energy band has Fano-type reso-

nances while the second sideband peaks have Breit-Wigner form. We also calculate numerically the AC Stark shift of the quasibound state position in the complex energy plane to show that the resonances move and broaden for stronger drive, as expected. Finally we present numerical results for the static component of conductance under a small source-drain bias with and without the AC drive with the latter displaying structures due to the resonances above. We also show first and second conductance harmonics, showing that the latter experiences resonant enhancement on quasibound state resonances, concluding that this can be used in a frequency doubler based on a ballistic graphene device.

My contribution to this work included development of the mathematical framework behind it together with O. Shevtsov. In particular, the description of the delta barrier in terms of the boundary condition and the bound state development was introduced by me in addition to the weak driving expansion. I contributed to the early drafts of the manuscript and the AC Stark shift chapter.

6.2 Paper II

Here we extend the model presented in Paper I. In addition to the delta barrier we include the effect of metallic electrodes doping graphene underneath by introducing a static piecewise-constant potential profile in our model Hamiltonian. In addition to the inelastic tunnelling resonances described in Paper I, the bound state is shown to be excited in the regime when evanescent modes are injected into the conducting medium from the doped regions, in the form of resonant double barrier tunnelling, see Chapter 3. We analyse the energy scales associated with the doping of leads and the channel, temperature and length of the device to establish different operation regimes of the device within experimental reach. We show that the static conductance response is strongly nonlinear with respect to the back gate potential in the vicinity of the bound state for strongly doped leads. Based on this we propose that such graphene-based device can be used for radiation detection in THz frequency range, for example if the gate signal is modulated by coupling it to an external antenna. We also extend the theory to a strong drive regime. We show how the dynamical delta barrier strength affects the coupling of the drive to individual sidebands via Bessel functions in the boundary condition. We demonstrate how multiple resonances appear in transmission to sidebands for low and high doping of

leads. For the case of high doping, we explore how double barrier tunnelling resonances form a ladder of equidistant transmission peaks with the period of one radiation quantum. Based on the fact that such ladders overlap for different sidebands as a function of channel doping, we demonstrate that higher ($n > 2$) conductance harmonics can be resonantly enhanced. Using the symmetry between individual scattering processes for absorbing and emitting the radiation quantum, we show that only even harmonics are enhanced. We therefore demonstrate theoretically a tunable frequency multiplication scheme based on channel doping and AC drive strength as control parameters, with higher harmonics available at stronger driving. It therefore builds on the result of Paper I allowing a single device used for higher multiplication factors in contrast to e.g. a cascaded scheme.

For this paper I expanded the model to include the doping profile of the device, described the resonant double barrier tunnelling regime, described coupling to sidebands in terms of Bessel functions, performed all the simulations and wrote the manuscript.

6.3 Paper III

In the third paper we describe shot noise performance of the proposed device. We use our Landauer-Büttiker formalism for Floquet states to describe current-current correlations. We focus on how resonances arising from different scattering mechanisms described in Papers I and II contribute to it. For dc operation we obtain a differential Fano factor of $1/3$ at minimal conductance due to Klein tunnelling, as has been established in the literature [138]. We examine how resonances in conductance and noise coincide but have opposite nature, i.e. peaks in conductance correspond to dips in noise as the back gate voltage is swept. We prove analytically that the noise is strongly suppressed at injection angles close to the normal incidence even for dynamic driving due to Klein tunnelling, which results in the overall noise figure being low. We examine the high and low doping regimes introduced in Paper II to analyse the noise properties of the proposed radiation detector and frequency multiplier. The frequency response of the detector is shown to have multiple peaks since the quasibound state can be excited by multiples of radiation quantum. The Fano factor is shown to be decreasing for higher multiples, while the peaks get narrower thus suggesting that the device's operation can be optimised considering the tradeoff between the response range and noise, e.g. the secondary

peak detection scheme might be favourable. We have also analysed the strong driving regime for both high and low doping of contacts, with the high doping consistently staying close to the pseudodiffusive value of $1/3$. The explanation comes from overlapping double barrier tunnelling resonance ladders similar to what we have described in Paper II, but for noise. Either all channels stay open or closed thus resulting in suppressed correlations. This is not the case for the low doping regime and Fano resonances thus resulting in stronger noise.

I performed all the simulations and wrote the manuscript of this paper. The analytical proof of the noise suppression under normal incidence was also done by me.

6.4 Paper IV

In the final paper of this thesis we turn to quantum pumping resulting from operation of the device in an asymmetric setup but with no source-drain bias applied. The asymmetry is achieved either via device geometry (placing the top gate closer to the source or the drain), or through different doping of the leads (e.g. different metals deposited for the source and the drain electrodes). We apply the established scattering matrix approach to demonstrate the effects of Fabry-Pérot interference and quasibound state resonances on the charge current pumped through the system. We show how Dirac cone cross sections at different energy sidebands, see Chapter 4, dictate the opening of scattering channels into the source and the drain. We show how identified scattering processes result in imbalance between current going in one direction or another. We show that Fabry-Pérot oscillations do not contribute for energies far away from the doping potential and only interaction with the quasibound state is the determining factor. The pump's response can therefore be tuned by the back gate. Since the transmission imbalance is quite antisymmetric with respect to the zero energy level, we have shown how Fermi functions of the reservoirs can result in the total pumped current changing direction, thus allowing for switching behaviour. Current magnitude can be controlled by tuning the back gate potential or by changing the device's temperature.

The simulations, data analysis and the manuscript were done by me.

Chapter 7

Summary and outlook

As a result of work presented in this thesis, we have developed a theory describing time-dependent quantum transport in a ballistic graphene device analogous to the original Landauer-Büttiker description of 2DEG. We have found a number of differences between our theory and the original arising due to the relativistic nature of charge carriers in graphene and the particular device setup that we describe.

We have applied the developed theory to describe current and noise in graphene FET. We identified a number of parameter regimes the transistor can be operated in and described scattering processes contributing to the charge current and noise in the device. We paid a lot of attention to inelastic scattering through a bound state leading to Fano and Breit-Wigner resonances in the context of applications in high-frequency electronics. Based on these resonances, we have suggested a frequency multiplication routine, which is not limited by a factor of two per device in contrast to the scheme used in graphene-based ambipolar mixers and amplifiers [139, 140]. We also put forward an idea of a radiation detector based on the resonant response of the transistor to the applied electric field and evaluated shot noise performance of the proposed devices. We confirmed that due to relativistic nature of charge carriers, the noise is suppressed also for high operational frequencies. We also proposed a single-parameter pumping routine based on interplay between Klein tunnelling and inelastic resonances present in the system. We think that ambipolar nature of the dispersion relation of graphene together with relativistic carriers and gate-tunable density of states provides more flexibility in design of the prospective devices. Advances in this fascinating area of study can enable

whole new types of devices developed for RF communication systems and electronics in general.

As this is a theory thesis, we tried to estimate relevant parameter regimes for experimental verification of our predictions to the best of our ability, however every model has its restrictions. Our conclusions are based effectively on a single-particle description of the system. As has been mentioned in the thesis, electron-electron interactions can play a role when impurity and phonon scattering is negligible. Incorporating them on the Hamiltonian level could be a step in the correct direction. Electron-electron interactions in graphene form a topic of their own [141]. On top of that we are considering a dynamical system in the sense that time-dependent current is pushed through the device. Thus, in principle, one should account for displacement currents and screening of charge by surrounding metallic surfaces. A self-consistent numerical solver of Maxwell's equations is likely to be a more cumbersome but also more realistic approach than the infinite parallel capacitor model we employed in our papers.

We saw that generally being based on quantum-mechanical resonances, the theory is sensitive to thermal fluctuations. In fact, reservoir temperature is incorporated into the developed formalism and effects of it on pumping have been studied in Paper IV, however further simulations are needed to describe it fully. The author envisions possibility of description of transport through the device in the presence of thermal gradient, which has not been done in the thesis.

Speaking of topics that the thesis did not touch upon, we can imagine combining the scattering theory developed here with static impurity scattering in graphene, where impurities can be described by Green's functions. Another possibility is to extend the formalism developed here to other two-dimensional systems or to degrees of freedom that were treated as degenerate here, with possible applications in spin- and valleytronics.

Let us conclude by saying that the rapidly evolving field of graphene and other two-dimensional materials keeps opening new directions of research and possibly still has many more surprises in its store.

Acknowledgements

Using the moment, I would like to express gratitude to my supervisor, Tomas Löfwander. I still wonder why after bearing with me over the master's thesis he chose another five years of babysitting. Deepest thanks for not giving up on me and trying to put some knowledge into my stubborn head. I am fortunate to have met Oleksii Shevtsov who acted as a part-time co-supervisor and without whom this work would not have been possible. He provided invaluable contribution to the project in both solid (state) physics advices and enthusiasm. I am thankful to all senior members at the lab: Vitaly Shumeiko for asking the right questions and sometimes telling me the answers, Mikael Fogelström, Göran Johansson, and Janine Splettstoesser for fruitful discussions and sharing their deep knowledge in physics.

It would have been very different without any of the junior members in the ever-growing AQP group. I appreciate all the sugar and science intake from the numerous Tuesday meetings and coffee breaks. I would like to thank my officemates Anders, Ian, Patric, and Emely for successfully simulating a hard-working atmosphere. Thanks to my colleagues in the QDP lab, e.g. Tom, Luca, Pier Paolo, André, Astghik, Gunta. Devices still blow up in my presence, but at least I know those able to tame them. Cheers to all FFF board 2014/15 members, it all went downhill after we quit. Thanks to all my other (imaginary) friends that I made (up) outside of academia. Whether it was traveling, ping-pong battles, climbing random round things or just kicking one round thing 90 minutes straight, I would do that again with you. I wouldn't have made it through without you. My warmest thoughts go to my family, I love you and regret not having spent more time with you.

I would also like to acknowledge the Swedish Institute for their support given through the Visby Program scholarship. If not for this funding, I

would not have been able to come to Sweden in the first place.

Dear reader, if you feel like your name is unjustifiedly missing above, it's because I reserved a special place for you in my heart.

Appendix A

Graphene tight-binding Hamiltonian

We can associate electrons on a simple Bravais lattice with a Hamiltonian

$$H = \frac{\mathbf{p}^2}{2m} + V(\mathbf{r} - \mathbf{R}_i), \quad (\text{A.1})$$

with the first part being kinetic energy and the last describing electrostatic potential associated with atomic sites R_i . One has to be careful since the particle cannot occupy a random position in space, but rather can only be translated by an arbitrary lattice vector under Bloch's theorem. Similarly, momentum \mathbf{p} is therefore restricted to the first Brillouin zone. This assumption is valid as long as the lattice is infinite, i.e. much larger than a single unit cell and the Fermi wavelength. Mass m is an effective band mass of an electron. However, in graphene we don't have a simple Bravais lattice. Therefore, due to the presence of two inequivalent sublattices, we have to present the electronic wave function as a superpositions of individual contributions from A and B

$$\psi_{\mathbf{k}}(\mathbf{r}) = A_{\mathbf{k}}\psi_{\mathbf{k},A}(\mathbf{r}) + B_{\mathbf{k}}\psi_{\mathbf{k},B}(\mathbf{r}), \quad (\text{A.2})$$

where complex coefficients A and B depend on wave vector \mathbf{k} , and sublattice Bloch wave functions

$$\psi_{\mathbf{k},\alpha} = \sum_{R_l} e^{i\mathbf{k}\cdot\mathbf{R}_l} \chi_{\alpha}(\mathbf{r} + \boldsymbol{\delta}_{\alpha} - \mathbf{R}_l), \quad \alpha = A,B, \quad (\text{A.3})$$

have an atomic component χ , and R_l defines atomic position in the constructed lattice. We already defined $\boldsymbol{\delta}_{\alpha}$ in (2.1), it connects position R_l

with atom α in the unit cell. We can set our Bravais lattice to sit on top of sublattice A by choosing $\delta_A = 0$.

Now we write down the Schrödinger equation for our system as

$$H\psi_{\mathbf{k}}(\mathbf{r}) = E_{\mathbf{k}}\psi_{\mathbf{k}}(\mathbf{r}), \quad \text{with } \psi_{\mathbf{k}}(\mathbf{r}) = \begin{pmatrix} A_{\mathbf{k}} & B_{\mathbf{k}} \end{pmatrix} \begin{pmatrix} \psi_{\mathbf{k},A}(\mathbf{r}) \\ \psi_{\mathbf{k},B}(\mathbf{r}) \end{pmatrix} \quad (\text{A.4})$$

By multiplying each side of the last equation with $\psi_{\mathbf{k}}^*(r)$ and integrating over space we can arrive at the form (omitting writing the integral and space dependence explicitly)

$$\begin{aligned} \begin{pmatrix} A_{\mathbf{k}}^* & B_{\mathbf{k}}^* \end{pmatrix} \mathcal{H}_{\mathbf{k}} \begin{pmatrix} A_{\mathbf{k}} \\ B_{\mathbf{k}} \end{pmatrix} &= E_{\mathbf{k}} \begin{pmatrix} A_{\mathbf{k}}^* & B_{\mathbf{k}}^* \end{pmatrix} \mathcal{S}_{\mathbf{k}} \begin{pmatrix} A_{\mathbf{k}} \\ B_{\mathbf{k}} \end{pmatrix} \\ \mathcal{H}_{\mathbf{k}} &= \begin{pmatrix} \psi_{\mathbf{k},A}^* H \psi_{\mathbf{k},A} & \psi_{\mathbf{k},A}^* H \psi_{\mathbf{k},B} \\ \psi_{\mathbf{k},B}^* H \psi_{\mathbf{k},A} & \psi_{\mathbf{k},B}^* H \psi_{\mathbf{k},B} \end{pmatrix} \\ \mathcal{S}_{\mathbf{k}} &= \begin{pmatrix} \psi_{\mathbf{k},A}^* \psi_{\mathbf{k},A} & \psi_{\mathbf{k},A}^* \psi_{\mathbf{k},B} \\ \psi_{\mathbf{k},B}^* \psi_{\mathbf{k},A} & \psi_{\mathbf{k},B}^* \psi_{\mathbf{k},B} \end{pmatrix} \end{aligned} \quad (\text{A.5})$$

At this point we will make a few assumptions in order to simplify the problem. We note that the normalization of wave function is just the number of particles $\int d\mathbf{r} \psi_{\mathbf{k},A}^* \psi_{\mathbf{k},A} = \int d\mathbf{r} \psi_{\mathbf{k},B}^* \psi_{\mathbf{k},B} = N$. We assume the overlap of orbitals on neighbouring sublattices to be negligibly small $\int d\mathbf{r} \psi_{\mathbf{k},A}^* \psi_{\mathbf{k},B} = \int d\mathbf{r} \psi_{\mathbf{k},B}^* \psi_{\mathbf{k},A} = 0$. Chemically, the sublattices A and B are completely equivalent, thus we are free to set the constant energy shift from the diagonal elements $\psi_{\mathbf{k},A}^* H \psi_{\mathbf{k},A} = \psi_{\mathbf{k},B}^* H \psi_{\mathbf{k},B}$ to zero. At this point we are left only with the off-diagonal terms $\mathcal{H}_{\mathbf{k}}^{AB} = \int d\mathbf{r} \psi_{\mathbf{k},A}^* H \psi_{\mathbf{k},B} = N t_{\mathbf{k}}^{AB}$, where the hopping term between sublattice A and B is given by

$$t_{\mathbf{k}}^{AB} = \sum_{\mathbf{R}_l} e^{i\mathbf{k} \cdot \mathbf{R}_l} \int d\mathbf{r} \chi_A^*(\mathbf{r} - \mathbf{R}_k) H \chi_B(\mathbf{r} + \boldsymbol{\delta}_{AB} - \mathbf{R}_m). \quad (\text{A.6})$$

In the simplest approximation that we will use here, one considers only nearest-neighbour hopping. In this case (A.6) becomes

$$t_{\mathbf{k}}^{AB} = t(1 + e^{-i\mathbf{k} \cdot \mathbf{a}_1} + e^{-i\mathbf{k} \cdot \mathbf{a}_2}), \quad t = \int d\mathbf{r} \chi_A^*(\mathbf{r}) H \chi_B(\mathbf{r} + \boldsymbol{\delta}_1). \quad (\text{A.7})$$

Here we include hopping to all three neighbours of atom A, with $\boldsymbol{\delta}_{AB} = \boldsymbol{\delta}_1$, and we use lattice vectors to account for the phase difference with the other two neighbouring B atoms. We note that $t_{AB} = t_{BA}^*$ and the number of

particles enters trivially, so it can be set to unity $N = 1$. Including all the assumptions into (A.5) we obtain

$$\mathcal{H}_{\mathbf{k}} = \begin{pmatrix} 0 & t_{\mathbf{k}}^{AB} \\ (t_{\mathbf{k}}^{AB})^* & 0 \end{pmatrix} \quad (\text{A.8})$$

$$\mathcal{S}_{\mathbf{k}} = \begin{pmatrix} 1 & 0 \\ 0 & 1 \end{pmatrix} \quad (\text{A.9})$$

Now we can obtain energy eigenvalues from the secular equation

$$\det |\mathcal{H}_{\mathbf{k}} - E_{\mathbf{k}} \mathcal{S}_{\mathbf{k}}| = 0 \quad \implies \quad \det \begin{vmatrix} -E_{\mathbf{k}} & t_{\mathbf{k}}^{AB} \\ (t_{\mathbf{k}}^{AB})^* & -E_{\mathbf{k}} \end{vmatrix} = 0. \quad (\text{A.10})$$

The solution gives two energy bands $E_{\mathbf{k}} = \pm |t_{\mathbf{k}}^{AB}|$.

Appendix B

Delta potential boundary condition

In this chapter we will show how a delta potential barrier can be presented as a limit of a short but high square barrier. We outline the procedure for both massive particles, described by the Schrödinger equation, and massless fermions, corresponding to the Dirac equation. It is done first for static scattering, and then extended for a time-periodic barrier. We assume a wavevector k_y in the direction along the barrier interface entering as a constant of motion, making this a quasi-1D problem.

B.1 Static barrier in Schrödinger equation

Taking the δ -function limit $D \rightarrow 0$ while $U_0 D = \frac{\hbar^2 Z_0}{2m} = \text{const}$ reduces the exponentials in (C.7) as

$$\begin{aligned} qD &\rightarrow 0 \\ q^2 D &\rightarrow -Z_0 \\ e^{iqD} &\rightarrow 1 \\ qe^{\pm iqD} &\rightarrow 1 \mp iZ_0. \end{aligned}$$

Thus the boundary condition (C.7) simplifies to

$$\left\{ \begin{array}{l} \begin{pmatrix} 1 \\ k \end{pmatrix} + r \begin{pmatrix} 1 \\ -k \end{pmatrix} = b \begin{pmatrix} 1 \\ q \end{pmatrix} + c \begin{pmatrix} 1 \\ -q \end{pmatrix} \\ t = b + c \\ tk = b(q - iZ_0) - c(q + iZ_0) \end{array} \right. \implies \left\{ \begin{array}{l} t = 1 + r \\ tk = (1 - r)k - iZ_0t. \end{array} \right. \quad (\text{B.1})$$

If we start with a δ barrier directly, see Fig. 3.2(b), the first derivative of the wave function has a finite jump. If we write down matching at the interface we arrive immediately at the boundary condition

$$\left\{ \begin{array}{l} t = 1 + r \\ ikt - ik(1 - r) = Z_0t, \end{array} \right. \quad (\text{B.2})$$

which is exactly the same as the one obtained from the limiting procedure applied after the boundary condition for the square barrier had been written. It proves that this δ -barrier representation is indeed the correct one in the limit. A completely analogous procedure is valid for derivation of a corresponding boundary condition for particles with linear dispersion relation. It is outlined in the next section.

B.2 Static barrier in Dirac equation

Take the delta limit $D \rightarrow 0$ with $Z = U_0D = \text{const}$ of the boundary condition (3.8) for the square barrier results in

$$\begin{aligned} q &\rightarrow -U_0 \rightarrow \infty \\ e^{iqD} &\rightarrow e^{-iZ_0} \\ \mu &\rightarrow 1 \\ \bar{\mu} &\rightarrow -1. \end{aligned}$$

The boundary condition reduces to

$$\left\{ \begin{array}{l} \begin{pmatrix} 1 \\ \eta \end{pmatrix} + r \begin{pmatrix} 1 \\ \bar{\eta} \end{pmatrix} = b \begin{pmatrix} 1 \\ 1 \end{pmatrix} + c \begin{pmatrix} 1 \\ -1 \end{pmatrix} \\ t \begin{pmatrix} 1 \\ \eta \end{pmatrix} = b \begin{pmatrix} 1 \\ 1 \end{pmatrix} e^{-iZ_0} + c \begin{pmatrix} 1 \\ -1 \end{pmatrix} e^{iZ_0}. \end{array} \right. \quad (\text{B.3})$$

The second equation actually can be rewritten in terms of a rotation matrix

$$\begin{cases} \begin{pmatrix} 1 \\ \eta \end{pmatrix} + r \begin{pmatrix} 1 \\ \bar{\eta} \end{pmatrix} = b \begin{pmatrix} 1 \\ 1 \end{pmatrix} + c \begin{pmatrix} 1 \\ -1 \end{pmatrix} \\ t \begin{pmatrix} 1 \\ \eta \end{pmatrix} = \begin{pmatrix} \cos Z_0 & -i \sin Z_0 \\ -i \sin Z_0 & \cos Z_0 \end{pmatrix} \cdot \left(b \begin{pmatrix} 1 \\ 1 \end{pmatrix} + c \begin{pmatrix} 1 \\ -1 \end{pmatrix} \right), \end{cases} \quad (\text{B.4})$$

that reduces the boundary condition to

$$\begin{pmatrix} 1 \\ \eta \end{pmatrix} + r \begin{pmatrix} 1 \\ \bar{\eta} \end{pmatrix} = \exp(iZ_0 \hat{\sigma}_x) t \begin{pmatrix} 1 \\ \eta \end{pmatrix}. \quad (\text{B.5})$$

The left-hand side of the equation contains the wave function to the left of the barrier, the right-hand side the transmitted wave, and they are just related via a rotation matrix $e^{iZ_0 \sigma_x}$. Physically it corresponds to the delta barrier redistributing the "weight" between A and B sublattice pseudospinor components of the wave passing through it.

B.3 Dynamic barrier in Schrödinger equation

We start directly with (4.17) derived in Chapter 4

$$\begin{cases} \delta_{n0} \begin{pmatrix} 1 \\ k_n \end{pmatrix} + r_n \begin{pmatrix} 1 \\ -k_n \end{pmatrix} = \sum_l \left[b_l \begin{pmatrix} 1 \\ q_l \end{pmatrix} + c_l \begin{pmatrix} 1 \\ -q_l \end{pmatrix} \right] J_{n-l} \left(\frac{U_1}{\hbar\Omega} \right) \\ t_n \begin{pmatrix} 1 \\ k_n \end{pmatrix} = \sum_l \left[b_l \begin{pmatrix} 1 \\ q_l \end{pmatrix} e^{iq_l D} + c_l \begin{pmatrix} 1 \\ -q_l \end{pmatrix} e^{-iq_l D} \right] J_{n-l} \left(\frac{U_1}{\hbar\Omega} \right) \end{cases} \quad (\text{B.6})$$

When taking a delta-function approximation here, one has to be careful with sums over sideband indices n, l since they run over infinity. In this limit, $D \rightarrow 0$ as $U_0 = \frac{\hbar^2 Z_0}{2m D}$ and $U_1 = \frac{\hbar^2 Z_1}{2m D}$, we get

$$\begin{aligned} q_l D &\rightarrow 0 \\ q_l^2 D &\rightarrow (l\hbar\Omega - U_0)D = l\hbar\Omega D - Z_0 \\ e^{iq_l D} &\rightarrow 1 \\ q_l e^{iq_l D} &\rightarrow q_l - iZ_0 + il\hbar\Omega D \end{aligned}$$

The boundary matching then is written as

$$\delta_{n0} + r_n = \sum_l (b_l + c_l) J_{n-l} \left(\frac{U_1}{\hbar\Omega} \right) \quad (\text{B.7})$$

$$k_n(\delta_{n0} - r_n) = \sum_l (b_l - c_l) q_l J_{n-l} \left(\frac{U_1}{\hbar\Omega} \right) \quad (\text{B.8})$$

$$t_n = \sum_l (b_l + c_l) J_{n-l} \left(\frac{U_1}{\hbar\Omega} \right) \quad (\text{B.9})$$

$$t_n k_n = \sum_l [(b_l - c_l) q_l + (b_l + c_l)(-iZ_0 + il\hbar\Omega D)] J_{n-l} \left(\frac{U_1}{\hbar\Omega} \right) \quad (\text{B.10})$$

Note that there are several terms ill-defined after we take the limit in this set of equations: q_l , $l\Omega D$ and Bessel functions $J_{n-l} \left(\frac{U_1}{\hbar\Omega} \right)$. The former terms can be eliminated by subtracting (B.8) from (B.10), and combining (B.7) and (B.9) gives

$$\begin{cases} \delta_{n0} + r_n = t_n \\ t_n = \sum_l (b_l + c_l) J_{n-l} \left(\frac{U_1}{\hbar\Omega} \right) \\ k_n(t_n - \delta_{n0} + r_n) = -iZ_0 t_n + \sum_l (b_l + c_l) il\hbar\Omega D J_{n-l} \left(\frac{U_1}{\hbar\Omega} \right) \end{cases} \quad (\text{B.11})$$

To overcome the uncertainty in $l\hbar\Omega D$ term we utilize a recurrence relation between Bessel functions of neighbouring sidebands

$$J_{n-l} \left(\frac{U_1}{\hbar\Omega} \right) = \frac{U_1/\hbar\Omega}{2(n-l)} \left[J_{n-l+1} \left(\frac{U_1}{\hbar\Omega} \right) + J_{n-l-1} \left(\frac{U_1}{\hbar\Omega} \right) \right] \quad (\text{B.12})$$

Combining it with the expansion term in question gives

$$\begin{aligned} l\hbar\Omega D J_{n-l} \left(\frac{U_1}{\hbar\Omega} \right) &= \frac{Z_1}{2} \frac{l}{n-l} \left[J_{n-l+1} \left(\frac{U_1}{\hbar\Omega} \right) + J_{n-l-1} \left(\frac{U_1}{\hbar\Omega} \right) \right] \\ &= \frac{Z_1}{2} \left(\frac{n}{n-l} - 1 \right) \left[J_{n-l+1} \left(\frac{U_1}{\hbar\Omega} \right) + J_{n-l-1} \left(\frac{U_1}{\hbar\Omega} \right) \right] \\ &= n\hbar\Omega D J_{n-l} \left(\frac{U_1}{\hbar\Omega} \right) - \frac{Z_1}{2} \left[J_{n-l+1} \left(\frac{U_1}{\hbar\Omega} \right) + J_{n-l-1} \left(\frac{U_1}{\hbar\Omega} \right) \right] \end{aligned} \quad (\text{B.13})$$

This may seem like a useless exercise until we plug the result back into (B.11) giving

$$\left\{ \begin{array}{l} \delta_{n0} + r_n = t_n \\ t_n = \sum_l (b_l + c_l) J_{n-l} \\ k_n(t_n - \delta_{n0} + r_n) = -iZ_0 t_n + \\ \quad + \sum_l (b_l + c_l) \left[in\hbar\Omega D J_{n-l} - i\frac{Z_1}{2}(J_{n-l+1} + J_{n-l-1}) \right] \end{array} \right.$$

Here we omit the Bessel functions argument for a more compact notation. Now we can get rid of the sum over sidebands in the last equation by substituting t_n instead, leaving

$$\left\{ \begin{array}{l} \delta_{n0} + r_n = t_n \\ t_n = \sum_l (b_l + c_l) J_{n-l} \\ k_n(t_n - \delta_{n0} + r_n) = -iZ_0 t_n - i\frac{Z_1}{2}(t_{n+1} + t_{n-1}) + in\hbar\Omega D t_n \end{array} \right.$$

Now the very last term can be safely disregarded as $D \rightarrow 0$ for any finite sideband index n , which leaves us with the boundary condition

$$\left\{ \begin{array}{l} \delta_{n0} + r_n = t_n \\ -2ik_n\delta_{n0} = (Z_0 - 2ik_n)t_n + \frac{Z_1}{2}(t_{n+1} + t_{n-1}), \end{array} \right. \quad (\text{B.14})$$

which is identical to the one presented by Bagwell [107] in Equation A1 of his paper. Also note how Bessel functions of U_1 disappeared from the final expression after we used substitution of waves inside the barrier in terms of the amplitudes outside of it.

A much faster approach is to start with the time-dependent Schrödinger equation after taking the delta-function limit

$$i\hbar \frac{\partial}{\partial t} \Psi(x, k_y, t) = \frac{\hbar^2}{2m} \left[-\nabla_x^2 + Z_0 \delta(x) + Z_1 \cos(\Omega t) \delta(x) \right] \Psi(x, k_y, t), \quad (\text{B.15})$$

and perform Fourier transform of it in the time domain giving

$$E\Psi(x, k_y, E) = \frac{\hbar^2}{2m} \left[(-\nabla_x^2 + Z_0 \delta(x))\Psi(x, k_y, E) + \frac{Z_1}{2} \delta(x) (\Psi(x, k_y, E + \Omega) + \Psi(x, k_y, E - \Omega)) \right]. \quad (\text{B.16})$$

Here we used the fact that $\cos \Omega t = \frac{1}{2}(e^{i\Omega t} + e^{-i\Omega t})$. Now integrating over $x \in [0^-, 0^+]$ gives us the boundary condition

$$0 = \nabla_x \left[\Psi(0^-, k_y, E) - \Psi(0^+, k_y, E) \right] + Z_0 \Psi(0, k_y, E) + \frac{Z_1}{2} \left[\Psi(0^-, k_y, E + \Omega) + \Psi(0^+, k_y, E - \Omega) \right] \quad (\text{B.17})$$

Inserting Floquet ansatz $\Psi(x, k_y, t) = \sum_n \psi_n(x, k_y) e^{-i(E/\hbar + n\Omega)t}$ one obtains

$$\nabla_x \left[\psi_n(0^+, k_y) - \psi_n(0^-, k_y) \right] = Z_0 \psi_n(0, k_y) + \frac{Z_1}{2} \left[\psi_{n-1}(0, k_y) + \psi_{n+1}(0, k_y) \right] \quad (\text{B.18})$$

Substituting scattering amplitudes from our propagating wave ansatz into here together with continuity of the wave function yields (B.14) as expected. This establishes that instead of deriving the boundary condition from the Schrödinger or Dirac equation for the square barrier and then taking the delta-function limit, it is more useful to apply the limit beforehand and then derive the boundary condition for the delta barrier if that is the goal. The latter procedure was therefore used in Chapter 4 for derivation of the boundary condition for the time-dependent Dirac equation, used in our papers.

Appendix C

Bound states in a square well

Here we derive conditions for bound state formation in a finite square well potential, first for Schrödinger equation (2DEG), and then for Dirac equation (graphene).

C.1 2DEG

The ansatz for the bound state calculation can then be written as

$$\psi(x) = \begin{cases} ae^{\kappa x} & x < 0 \\ be^{iqx} + ce^{-iqx}, & 0 < x < D \\ de^{-\kappa x}, & x > D, \end{cases} \quad (\text{C.1})$$

where $\kappa = -ik \in \Re$ for the setup of Section 3.1.1. Wave function and first derivative continuity dictates the boundary condition

$$\begin{cases} a \begin{pmatrix} 1 \\ \kappa \end{pmatrix} = b \begin{pmatrix} 1 \\ iq \end{pmatrix} + c \begin{pmatrix} 1 \\ -iq \end{pmatrix} \\ d \begin{pmatrix} 1 \\ -\kappa \end{pmatrix} e^{-\kappa D} = b \begin{pmatrix} 1 \\ iq \end{pmatrix} e^{iqD} + c \begin{pmatrix} 1 \\ -iq \end{pmatrix} e^{-iqD}. \end{cases} \quad (\text{C.2})$$

The first equation line can be used to eliminate amplitudes a and c , while the second to eliminate d and b , leaving

$$-\kappa = iq \frac{(iq + \kappa)e^{iqD} - (iq - \kappa)e^{-iqD}}{(iq + \kappa)e^{iqD} + (iq + \kappa)e^{-iqD}} \quad (\text{C.3})$$

It can be rewritten in a quadratic form

$$q^2 - 2\kappa q \cot(qD) - \kappa^2 = 0, \quad (\text{C.4})$$

which leaves us with two possible "solutions"

$$q = \kappa \cot(qD/2) \quad (\text{C.5})$$

$$q = -\kappa \tan(qD/2). \quad (\text{C.6})$$

Each of these equations is in general non-algebraic and defines the even and odd bound states in the well respectively.

C.2 Graphene

We start directly with a boundary condition for graphene here,

$$\begin{cases} a \begin{pmatrix} 1 \\ \bar{\eta} \end{pmatrix} = b \begin{pmatrix} 1 \\ \mu \end{pmatrix} + c \begin{pmatrix} 1 \\ \bar{\mu} \end{pmatrix} \\ d \begin{pmatrix} 1 \\ \eta \end{pmatrix} e^{-\kappa D} = b \begin{pmatrix} 1 \\ \mu \end{pmatrix} e^{iqD} + c \begin{pmatrix} 1 \\ \bar{\mu} \end{pmatrix} e^{-iqD}. \end{cases} \quad (\text{C.7})$$

Eliminating amplitudes a and c from the first equation, and b and d from the second, we obtain

$$\eta = \frac{-\frac{1+\bar{\eta}\mu}{\bar{\eta}-\mu} e^{iqD} + \bar{\mu} e^{-iqD}}{\frac{\mu-\bar{\eta}}{\bar{\eta}-\mu} e^{iqD} + e^{-iqD}}. \quad (\text{C.8})$$

After multiplying the terms using $\eta\bar{\eta} = \mu\bar{\mu} = -1$, we obtain

$$(2 + \eta\bar{\mu} + \mu\bar{\eta})e^{iqD} = (2 + \bar{\eta}\bar{\mu} + \mu\eta)e^{-iqD}, \quad (\text{C.9})$$

which can then be rewritten in the form (3.18).

Appendix D

Commutation relations

Here we use convention for the Dirac delta function

$$\delta(k) = \frac{1}{2\pi} \int_{-\infty}^{\infty} e^{ikx} dx. \quad (\text{D.1})$$

We note that the Dirac delta function makes physical sense only when defined under an integral sign or viewed as a limit of a distribution. Using (5.15) and (5.14) we can write

$$\begin{aligned} \{\hat{a}_n(k), \hat{a}_m^\dagger(k')\} &= e^{i(E_n(k) - E_m(k'))t/\hbar} \{\hat{a}_n(k, t), \hat{a}_m^\dagger(k', t')\} = \\ &= \frac{1}{2\pi} \iiint\!\!\!\int dx dy dx' dy' \psi_y^n(y) \psi_{y'}^{m*}(y') e^{-ikx + ik'x'} \hat{\Psi}(x, y, t), \hat{\Psi}^\dagger(x', y', t) \\ &= \frac{1}{2\pi} \iiint\!\!\!\int dx dy dx' dy' \psi_y^n(y) \psi_{y'}^{m*}(y') e^{-ikx + ik'x'} \delta(x - x') \delta(y - y') \\ &= \frac{1}{2\pi} \iint dx dy \psi_y^n(y) \psi_y^{m*}(y) e^{-ikx + ik'x} = \delta(k - k') \delta_{nm}. \end{aligned}$$

Here we used the orthonormality condition for transverse waves and the definition of the delta function. Now we can do the same in the energy representation of the operators

$$\begin{aligned} \{\hat{a}_n(E), \hat{a}_m^\dagger(E')\} &= \frac{1}{\hbar \sqrt{v_n(E) v_m(E')}} \{\hat{a}_n(k), \hat{a}_m^\dagger(k')\} \\ &= \frac{1}{\hbar \sqrt{v_n(E) v_m(E')}} \delta_{nm} \delta \left(\frac{\sqrt{2m(E - E_y^n)}}{\hbar} - \frac{\sqrt{2m(E' - E_y^m)}}{\hbar} \right) \\ &= \delta_{nm} \delta(E - E'). \end{aligned}$$

Here we used the property $\delta(g(x)) = \frac{\delta(x-x_0)}{|\frac{dg}{dx}(x_0)|}$ if x_0 is the real root of $g(x)=0$.

Appendix E

Fermi-Dirac distribution limits

Let us consider Fermi distributions in leads L,R under an external bias V_{LR} given by

$$f_{L,R} = \frac{1}{1 + e^{(E - E_F + eV_{L,R})/k_B\Xi}} \quad (\text{E.1})$$

In the limit of zero temperature they become step functions

$$\lim_{\Xi \rightarrow 0} f_{L,R} = 1 - \theta(E - E_F - eV_{L,R}). \quad (\text{E.2})$$

Now we can assume the voltage bias to be small, and expand the expression above to the first order in it, giving

$$f_{L,R} = 1 - \theta(E - E_F) + eV_{L,R}\delta(E - E_F) + \mathcal{O}(V_{L,R}^2) \quad (\text{E.3})$$

The difference between them is therefore

$$f_L - f_R = eV_{LR}\delta(E - E_F) \quad (\text{E.4})$$

Applying the same procedure to the square of the difference leaves us with the same result since

$$\begin{aligned} (f_L - f_R)^2 &= \{1 - \theta(E - E_F - eV_L) - [1 - \theta(E - E_F - eV_R)]\}^2 = \\ &= |\theta(E - E_F - eV_R) - \theta(E - E_F - eV_L)|. \end{aligned} \quad (\text{E.5})$$

Here we used that the square of theta function is itself. This last formula is applicable to the noise derivation we have in Paper III.

Bibliography

- [1] P. R. Wallace, “The band theory of graphite”, *Physical Review* **71**, 622 (1947).
- [2] G. W. Semenoff, “Condensed-matter simulation of a three-dimensional anomaly”, *Physical Review Letters* **53**, 2449 (1984).
- [3] K. S. Novoselov, A. K. Geim, S. V. Morozov, D. Jiang, Y. Zhang, S. V. Dubonos, I. V. Grigorieva, and A. A. Firsov, “Electric field effect in atomically thin carbon films”, *Science* **306**, 666 (2004).
- [4] K. S. Novoselov, A. K. Geim, S. Morozov, D. Jiang, M. Katsnelson, I. Grigorieva, S. Dubonos, and A. Firsov, “Two-dimensional gas of massless dirac fermions in graphene”, *nature* **438**, 197 (2005).
- [5] V. V. Cheianov, V. Fal’ko, and B. Altshuler, “The focusing of electron flow and a veselago lens in graphene pn junctions”, *Science* **315**, 1252 (2007).
- [6] A. F. Young and P. Kim, “Quantum interference and klein tunnelling in graphene heterojunctions”, *Nature Physics* **5**, 222 (2009).
- [7] C. Lee, X. Wei, J. W. Kysar, and J. Hone, “Measurement of the elastic properties and intrinsic strength of monolayer graphene”, *science* **321**, 385 (2008).
- [8] A. A. Balandin, S. Ghosh, W. Bao, I. Calizo, D. Teweldebrhan, F. Miao, and C. N. Lau, “Superior thermal conductivity of single-layer graphene”, *Nano letters* **8**, 902 (2008).
- [9] M. D. Stoller, S. Park, Y. Zhu, J. An, and R. S. Ruoff, “Graphene-based ultracapacitors”, *Nano letters* **8**, 3498 (2008).
- [10] B. Lalmi, H. Oughaddou, H. Enriquez, A. Kara, S. Vizzini, B. Ealet, and B. Aufray, “Epitaxial growth of a silicene sheet”, *Applied Physics Letters* **97**, 223109 (2010).
- [11] Z. Ni, Q. Liu, K. Tang, J. Zheng, J. Zhou, R. Qin, Z. Gao, D. Yu, and J. Lu, “Tunable bandgap in silicene and germanene”, *Nano Letters* **12**, 113 (2011).

- [12] C. R. Dean, A. F. Young, I. Meric, C. Lee, L. Wang, S. Sorgenfrei, K. Watanabe, T. Taniguchi, P. Kim, K. L. Shepard, et al., “Boron nitride substrates for high-quality graphene electronics”, *Nature nanotechnology* **5**, 722 (2010).
- [13] H Zhang, S. Lu, J Zheng, J Du, S. Wen, D. Tang, and K. Loh, “Molybdenum disulfide (mos 2) as a broadband saturable absorber for ultra-fast photonics”, *Optics express* **22**, 7249 (2014).
- [14] L Britnell, R. Gorbachev, R Jalil, B. Belle, F Schedin, A Mishchenko, T Georgiou, M. Katsnelson, L Eaves, S. Morozov, et al., “Field-effect tunneling transistor based on vertical graphene heterostructures”, *Science* **335**, 947 (2012).
- [15] W. Zhang, C.-P. Chuu, J.-K. Huang, C.-H. Chen, M.-L. Tsai, Y.-H. Chang, C.-T. Liang, Y.-Z. Chen, Y.-L. Chueh, J.-H. He, et al., “Ultrahigh-gain photodetectors based on atomically thin graphene-mos2 heterostructures”, *Scientific reports* **4**, 3826 (2014).
- [16] M. J. Allen, V. C. Tung, and R. B. Kaner, “Honeycomb carbon: a review of graphene”, *Chemical reviews* **110**, 132 (2009).
- [17] A. C. Neto, F Guinea, N. M. Peres, K. S. Novoselov, and A. K. Geim, “The electronic properties of graphene”, *Reviews of modern physics* **81**, 109 (2009).
- [18] S. D. Sarma, S. Adam, E. Hwang, and E. Rossi, “Electronic transport in two-dimensional graphene”, *Reviews of Modern Physics* **83**, 407 (2011).
- [19] A. Grigorenko, M. Polini, and K. Novoselov, “Graphene plasmonics”, *Nature photonics* **6**, 749 (2012).
- [20] P. Rickhaus, P. Makk, M.-H. Liu, E. Tóvári, M. Weiss, R. Maurand, K. Richter, and C. Schönenberger, “Snake trajectories in ultraclean graphene p–n junctions”, *Nature communications* **6** (2015).
- [21] Y. Zhao, J. Wyrick, F. D. Natterer, J. F. Rodriguez-Nieva, C. Lewandowski, K. Watanabe, T. Taniguchi, L. S. Levitov, N. B. Zhitenev, and J. A. Stroscio, “Creating and probing electron whispering-gallery modes in graphene”, *Science* **348**, 672 (2015).
- [22] D. Bandurin, I Torre, R. K. Kumar, M. B. Shalom, A Tomadin, A Principi, G. Auton, E Khestanova, K. Novoselov, I. Grigorieva, et al., “Negative local resistance caused by viscous electron backflow in graphene”, *Science* **351**, 1055 (2016).
- [23] J. Crossno, J. K. Shi, K. Wang, X. Liu, A. Harzheim, A. Lucas, S. Sachdev, P. Kim, T. Taniguchi, K. Watanabe, et al., “Observation of the dirac fluid and the breakdown of the wiedemann-franz law in graphene”, *Science* **351**, 1058 (2016).

- [24] Y.-M. Lin, C. Dimitrakopoulos, K. A. Jenkins, D. B. Farmer, H.-Y. Chiu, A. Grill, and P. Avouris, “100-ghz transistors from wafer-scale epitaxial graphene”, *Science* **327**, 662 (2010).
- [25] S.-J. Han, K. A. Jenkins, A. Valdes Garcia, A. D. Franklin, A. A. Bol, and W. Haensch, “High-frequency graphene voltage amplifier”, *Nano letters* **11**, 3690 (2011).
- [26] F. Koppens, T Mueller, P. Avouris, A. Ferrari, M. Vitiello, and M Polini, “Photodetectors based on graphene, other two-dimensional materials and hybrid systems”, *Nature nanotechnology* **9**, 780 (2014).
- [27] G. P. Williams, “Filling the thz gap—high power sources and applications”, *Reports on Progress in Physics* **69**, 301 (2005).
- [28] M Büttiker, “Scattering theory of current and intensity noise correlations in conductors and wave guides”, *Physical Review B* **46**, 12485 (1992).
- [29] S. Reich, J. Maultzsch, C. Thomsen, and P. Ordejon, “Tight-binding description of graphene”, *Physical Review B* **66**, 035412 (2002).
- [30] R. Deacon, K.-C. Chuang, R. Nicholas, K. Novoselov, and A. Geim, “Cyclotron resonance study of the electron and hole velocity in graphene monolayers”, *Physical Review B* **76**, 081406 (2007).
- [31] Y.-W. Son, M. L. Cohen, and S. G. Louie, “Energy gaps in graphene nanoribbons”, *Physical Review Letters* **97**, 216803 (2006).
- [32] L. Landau, “Zur theorie der phasenumwandlungen II”, *Phys. Z. Sowjetunion* **11**, 26 (1937).
- [33] K. S. Novoselov, “Nobel lecture: graphene: materials in the flatland”, *Rev. Mod. Phys.* **83**, 837 (2011).
- [34] J. C. Meyer, A. K. Geim, M. I. Katsnelson, K. S. Novoselov, T. J. Booth, and S. Roth, “The structure of suspended graphene sheets”, *Nature* **446**, 60 (2007).
- [35] F. Bonaccorso, A. Lombardo, T. Hasan, Z. Sun, L. Colombo, and A. C. Ferrari, “Production and processing of graphene and 2d crystals”, *Materials Today* **15**, 564 (2012).
- [36] L. Girifalco and R. Lad, “Energy of cohesion, compressibility, and the potential energy functions of the graphite system”, *The Journal of Chemical Physics* **25**, 693 (1956).
- [37] www.grapheneindustries.com.
- [38] C. Dean, A. Young, P. Cadden-Zimansky, L Wang, H Ren, K Watanabe, T Taniguchi, P Kim, J Hone, and K. Shepard, “Multicomponent fractional quantum hall effect in graphene”, *Nature Physics* **7**, 693 (2011).

- [39] R Danneau, F Wu, M. Craciun, S Russo, M. Tomi, J Salmilehto, A. Morpurgo, and P. J. Hakonen, "Shot noise in ballistic graphene", *Physical Review Letters* **100**, 196802 (2008).
- [40] Y. Hernandez, V. Nicolosi, M. Lotya, F. M. Blighe, Z. Sun, S. De, I. McGovern, B. Holland, M. Byrne, Y. K. Gun'Ko, et al., "High-yield production of graphene by liquid-phase exfoliation of graphite", *Nature Nanotechnology* **3**, 563 (2008).
- [41] V. Nicolosi, M. Chhowalla, M. G. Kanatzidis, M. S. Strano, and J. N. Coleman, "Liquid exfoliation of layered materials", *Science* **340**, 1226419 (2013).
- [42] S. Park and R. S. Ruoff, "Chemical methods for the production of graphenes", *Nature Nanotechnology* **4**, 217 (2009).
- [43] M. Lotya, Y. Hernandez, P. J. King, R. J. Smith, V. Nicolosi, L. S. Karlsson, F. M. Blighe, S. De, Z. Wang, I. McGovern, et al., "Liquid phase production of graphene by exfoliation of graphite in surfactant/water solutions", *Journal of the American Chemical Society* **131**, 3611 (2009).
- [44] D. Nuvoli, L. Valentini, V. Alzari, S. Scognamillo, S. B. Bon, M. Piccinini, J. Illescas, and A. Mariani, "High concentration few-layer graphene sheets obtained by liquid phase exfoliation of graphite in ionic liquid", *Journal of Materials Chemistry* **21**, 3428 (2011).
- [45] J. R. Lomeda, C. D. Doyle, D. V. Kosynkin, W.-F. Hwang, and J. M. Tour, "Diazonium functionalization of surfactant-wrapped chemically converted graphene sheets", *Journal of the American Chemical Society* **130**, 16201 (2008).
- [46] X. Zhou and Z. Liu, "A scalable, solution-phase processing route to graphene oxide and graphene ultralarge sheets", *Chemical Communications* **46**, 2611 (2010).
- [47] A. B. Bourlinos, V. Georgakilas, R. Zboril, T. A. Steriotis, and A. K. Stubos, "Liquid-phase exfoliation of graphite towards solubilized graphenes", *Small* **5**, 1841 (2009).
- [48] W. S. Hummers Jr and R. E. Offeman, "Preparation of graphitic oxide", *Journal of the American Chemical Society* **80**, 1339 (1958).
- [49] S. Stankovich, D. A. Dikin, G. H. Dommett, K. M. Kohlhaas, E. J. Zimney, E. A. Stach, R. D. Piner, S. T. Nguyen, and R. S. Ruoff, "Graphene-based composite materials", *Nature* **442**, 282 (2006).
- [50] S. Stankovich, R. D. Piner, X. Chen, N. Wu, S. T. Nguyen, and R. S. Ruoff, "Stable aqueous dispersions of graphitic nanoplatelets via the reduction of exfoliated graphite oxide in the presence of poly (sodium 4-styrenesulfonate)", *Journal of Materials Chemistry* **16**, 155 (2006).

- [51] C. Gómez-Navarro, M. Burghard, and K. Kern, “Elastic properties of chemically derived single graphene sheets”, *Nano lett* **8**, 2045 (2008).
- [52] H. C. Schniepp, J.-L. Li, M. J. McAllister, H. Sai, M. Herrera-Alonso, D. H. Adamson, R. K. Prud’homme, R. Car, D. A. Saville, and I. A. Aksay, “Functionalized single graphene sheets derived from splitting graphite oxide”, *The Journal of Physical Chemistry B* **110**, 8535 (2006).
- [53] M. J. McAllister, J.-L. Li, D. H. Adamson, H. C. Schniepp, R. Car, R. K. Prud’homme, and I. A. Aksay, “Single sheet functionalized graphene by oxidation and thermal expansion of graphite”, *Nature* **442**, 282 (2006).
- [54] X. Li, W. Cai, J. An, S. Kim, J. Nah, D. Yang, R. Piner, A. Velamakanni, I. Jung, E. Tutuc, et al., “Large-area synthesis of high-quality and uniform graphene films on copper foils”, *Science* **324**, 1312 (2009).
- [55] S. Bae, H. Kim, Y. Lee, X. Xu, J.-S. Park, Y. Zheng, J. Balakrishnan, T. Lei, H. R. Kim, Y. I. Song, et al., “Roll-to-roll production of 30-inch graphene films for transparent electrodes”, *Nature Nanotechnology* **5**, 574 (2010).
- [56] L. Gao, W. Ren, H. Xu, L. Jin, Z. Wang, T. Ma, L.-P. Ma, Z. Zhang, Q. Fu, L.-M. Peng, et al., “Repeated growth and bubbling transfer of graphene with millimetre-size single-crystal grains using platinum”, *Nature Communications* **3**, 699 (2012).
- [57] M. Wang, S. K. Jang, W.-J. Jang, M. Kim, S.-Y. Park, S.-W. Kim, S.-J. Kahng, J.-Y. Choi, R. S. Ruoff, Y. J. Song, et al., “A platform for large-scale graphene electronics—cvd growth of single-layer graphene on cvd-grown hexagonal boron nitride”, *Advanced Materials* **25**, 2746 (2013).
- [58] L. Banszerus, M. Schmitz, S. Engels, M. Goldsche, K. Watanabe, T. Taniguchi, B. Beschoten, and C. Stampfer, “Ballistic transport exceeding 28 μm in cvd grown graphene”, *Nano Letters* **16**, PMID: 26761190, 1387 (2016).
- [59] C. Virojanadara, M. Syväjarvi, R. Yakimova, L. Johansson, A. Zakharov, and T. Balasubramanian, “Homogeneous large-area graphene layer growth on 6 h-sic (0001)”, *Physical Review B* **78**, 245403 (2008).
- [60] X. Wu, Y. Hu, M. Ruan, N. K. Madiomanana, J. Hankinson, M. Sprinkle, C. Berger, and W. A. De Heer, “Half integer quantum hall effect in high mobility single layer epitaxial graphene”, *Applied Physics Letters* **95**, 223108 (2009).
- [61] K. V. Emtsev, A. Bostwick, K. Horn, J. Jobst, G. L. Kellogg, L. Ley, J. L. McChesney, T. Ohta, S. A. Reshanov, J. Röhr, et al., “Towards wafer-size graphene layers by atmospheric pressure graphitization of silicon carbide”, *Nature Materials* **8**, 203 (2009).

- [62] K. Emtsev, F. Speck, T. Seyller, L. Ley, and J. D. Riley, "Interaction, growth, and ordering of epitaxial graphene on sic {0001} surfaces: a comparative photoelectron spectroscopy study", *Physical Review B* **77**, 155303 (2008).
- [63] C. Riedl, A. Zakharov, and U. Starke, "Precise in situ thickness analysis of epitaxial graphene layers on sic (0001) using low-energy electron diffraction and angle resolved ultraviolet photoelectron spectroscopy", *Applied Physics Letters* **93**, 033106 (2008).
- [64] S. Kopylov, A. Tzalenchuk, S. Kubatkin, and V. I. Fal'ko, "Charge transfer between epitaxial graphene and silicon carbide", *Applied Physics Letters* **97**, 112109 (2010).
- [65] order.universitywafer.com.
- [66] G. Eda, G. Fanchini, and M. Chhowalla, "Large-area ultrathin films of reduced graphene oxide as a transparent and flexible electronic material", *Nature Nanotechnology* **3**, 270 (2008).
- [67] X. Wang, L. Zhi, N. Tsao, Ž. Tomović, J. Li, and K. Müllen, "Transparent carbon films as electrodes in organic solar cells", *Angewandte Chemie* **120**, 3032 (2008).
- [68] Y. Zhang, L. Zhang, and C. Zhou, "Review of chemical vapor deposition of graphene and related applications", *Accounts of chemical research* **46**, 2329 (2013).
- [69] J. Alexander-Webber, A. Baker, T. Janssen, A. Tzalenchuk, S. Lara-Avila, S. Kubatkin, R. Yakimova, B. Piot, D. Maude, and R. Nicholas, "Phase space for the breakdown of the quantum hall effect in epitaxial graphene", *Physical Review Letters* **111**, 096601 (2013).
- [70] A. Lartsev, S. Lara-Avila, A. Danilov, S. Kubatkin, A. Tzalenchuk, and R. Yakimova, "A prototype of $h/200$ quantum hall array resistance standard on epitaxial graphene", *Journal of Applied Physics* **118**, 044506 (2015).
- [71] Y. Taur and T. H. Ning, *Fundamentals of modern vlsi devices* (Cambridge university press, 2013).
- [72] Q. Zhang, Y. Lu, H. G. Xing, S. J. Koester, and S. O. Koswatta, "Scalability of atomic-thin-body (atb) transistors based on graphene nanoribbons", *IEEE Electron Device Letters* **31**, 531 (2010).
- [73] E. Hwang and S. D. Sarma, "Acoustic phonon scattering limited carrier mobility in two-dimensional extrinsic graphene", *Physical Review B* **77**, 115449 (2008).
- [74] K. I. Bolotin, K. Sikes, Z. Jiang, M. Klima, G. Fudenberg, J. Hone, P. Kim, and H. Stormer, "Ultrahigh electron mobility in suspended graphene", *Solid State Communications* **146**, 351 (2008).

- [75] I. Aberg and J. L. Hoyt, "Hole transport in utb mosfets in strained-si directly on insulator with strained-si thickness less than 5 nm", *IEEE electron device letters* **26**, 661 (2005).
- [76] M. Y. Han, B. Özyilmaz, Y. Zhang, and P. Kim, "Energy band-gap engineering of graphene nanoribbons", *Physical Review Letters* **98**, 206805 (2007).
- [77] X. Li, X. Wang, L. Zhang, S. Lee, and H. Dai, "Chemically derived, ultra-smooth graphene nanoribbon semiconductors", *Science* **319**, 1229 (2008).
- [78] Z. H. Ni, T. Yu, Y. H. Lu, Y. Y. Wang, Y. P. Feng, and Z. X. Shen, "Uniaxial strain on graphene: raman spectroscopy study and bandgap opening", *arXiv preprint arXiv:0810.3476* (2008).
- [79] Y. Zhang, T.-T. Tang, C. Girit, Z. Hao, M. C. Martin, A. Zettl, M. F. Crommie, Y. R. Shen, and F. Wang, "Direct observation of a widely tunable bandgap in bilayer graphene", *Nature* **459**, 820 (2009).
- [80] J. A. Kelber, M. Zhou, S. Gaddam, F. L. Pasquale, L. M. Kong, and P. A. Dowben, "Direct graphene growth on oxides: interfacial interactions and band gap formation", *ECS Transactions* **45**, 49 (2012).
- [81] H. Raza and E. C. Kan, "Armchair graphene nanoribbons: electronic structure and electric-field modulation", *Physical Review B* **77**, 245434 (2008).
- [82] B. Obradovic, R. Kotlyar, F. Heinz, P. Matagne, T. Rakshit, M. Giles, M. Stettler, and D. Nikonov, "Analysis of graphene nanoribbons as a channel material for field-effect transistors", *Applied Physics Letters* **88**, 142102 (2006).
- [83] M.-W. Lin, C. Ling, L. A. Agapito, N. Kioussis, Y. Zhang, M. M.-C. Cheng, W. L. Wang, E. Kaxiras, and Z. Zhou, "Approaching the intrinsic band gap in suspended high-mobility graphene nanoribbons", *Physical Review B* **84**, 125411 (2011).
- [84] B. Radisavljevic, A. Radenovic, J. Brivio, i. V. Giacometti, and A. Kis, "Single-layer mos2 transistors", *Nature Nanotechnology* **6**, 147 (2011).
- [85] S. B. Desai, S. R. Madhvapathy, A. B. Sachid, J. P. Llinas, Q. Wang, G. H. Ahn, G. Pitner, M. J. Kim, J. Bokor, C. Hu, et al., "Mos2 transistors with 1-nanometer gate lengths", *Science* **354**, 99 (2016).
- [86] V. E. Dorgan, M.-H. Bae, and E. Pop, "Mobility and saturation velocity in graphene on sio 2", *Applied Physics Letters* **97**, 082112 (2010).
- [87] Y. Wu, K. A. Jenkins, A. Valdes-Garcia, D. B. Farmer, Y. Zhu, A. A. Bol, C. Dimitrakopoulos, W. Zhu, F. Xia, P. Avouris, et al., "State-of-the-art graphene high-frequency electronics", *Nano letters* **12**, 3062 (2012).
- [88] F. Schwierz, "Graphene transistors: status, prospects, and problems", *Proceedings of the IEEE* **101**, 1567 (2013).

- [89] Y.-M. Lin, A. Valdes-Garcia, S.-J. Han, D. B. Farmer, I. Meric, Y. Sun, Y. Wu, C. Dimitrakopoulos, A. Grill, P. Avouris, et al., “Wafer-scale graphene integrated circuit”, *Science* **332**, 1294 (2011).
- [90] H. Kroemer, “Quantum mechanics for engineering”, *Materials Science and Applied Physics* (Prentice-Hall, 1994) (1994).
- [91] O. Klein, “Die reflexion von elektronen an einem potentialsprung nach der relativistischen dynamik von dirac”, *Zeitschrift für Physik* **53**, 157 (1929).
- [92] A Calogeracos and N. Dombey, “History and physics of the klein paradox”, *Contemporary physics* **40**, 313 (1999).
- [93] M. Katsnelson, K. Novoselov, and A. Geim, “Chiral tunnelling and the klein paradox in graphene”, *Nature physics* **2**, 620 (2006).
- [94] H. Wang, A. Hsu, K. K. Kim, J. Kong, and T. Palacios, “Gigahertz ambipolar frequency multiplier based on cvd graphene”, in *Electron devices meeting (iedm), 2010 ieee international (IEEE, 2010)*, pp. 23–6.
- [95] R Tsu and L. Esaki, “Tunneling in a finite superlattice”, *Applied Physics Letters* **22**, 562 (1973).
- [96] H. Yamamoto, “Resonant tunneling condition and transmission coefficient in a symmetrical one-dimensional rectangular double-barrier system”, *Applied Physics A* **42**, 245 (1987).
- [97] U. Gennser, V. Kesan, S. Iyer, T. Buecelot, and E. Yang, “Resonant tunneling of holes through silicon barriers”, *Journal of Vacuum Science & Technology B: Microelectronics Processing and Phenomena* **8**, 210 (1990).
- [98] N. Orihashi, S. Suzuki, and M. Asada, “One thz harmonic oscillation of resonant tunneling diodes”, *Applied Physics Letters* **87**, 233501 (2005).
- [99] M. Asada, S. Suzuki, and N. Kishimoto, “Resonant tunneling diodes for sub-terahertz and terahertz oscillators”, *Japanese Journal of Applied Physics* **47**, 4375 (2008).
- [100] J. M. Pereira Jr, P Vasilopoulos, and F. Peeters, “Graphene-based resonant-tunneling structures”, *Applied physics letters* **90**, 132122 (2007).
- [101] V. H. Nguyen, F. Mazzamuto, A. Bournel, and P. Dollfus, “Resonant tunnelling diodes based on graphene/h-bn heterostructure”, *Journal of Physics D: Applied Physics* **45**, 325104 (2012).
- [102] G. Giovannetti, P. Khomyakov, G Brocks, V. v. Karpan, J Van den Brink, and P. Kelly, “Doping graphene with metal contacts”, *Physical Review Letters* **101**, 026803 (2008).
- [103] P Blake, R Yang, S. Morozov, F Schedin, L. Ponomarenko, A. Zhukov, R. Nair, I. Grigorieva, K. Novoselov, and A. Geim, “Influence of metal contacts and charge inhomogeneity on transport properties of graphene near the neutrality point”, *Solid State Communications* **149**, 1068 (2009).

- [104] L. Britnell, R. Gorbachev, A. Geim, L. Ponomarenko, A. Mishchenko, M. Greenaway, T. Fromhold, K. Novoselov, and L. Eaves, “Resonant tunnelling and negative differential conductance in graphene transistors”, *Nature Communications* **4**, 1794 (2013).
- [105] P. Tien and J. Gordon, “Multiphoton process observed in the interaction of microwave fields with the tunneling between superconductor films”, *Physical Review* **129**, 647 (1963).
- [106] W. Li and L. Reichl, “Floquet scattering through a time-periodic potential”, *Physical Review B* **60**, 15732 (1999).
- [107] P. F. Bagwell and R. K. Lake, “Resonances in transmission through an oscillating barrier”, *Physical Review B* **46**, 15329 (1992).
- [108] A. E. Miroschnichenko, S. Flach, and Y. S. Kivshar, “Fano resonances in nanoscale structures”, *Reviews of Modern Physics* **82**, 2257 (2010).
- [109] U. Fano, “Sullo spettro di assorbimento dei gas nobili presso il limite dello spettro d’arco”, *Il Nuovo Cimento (1924-1942)* **12**, 154 (1935).
- [110] U. Fano, “Effects of configuration interaction on intensities and phase shifts”, *Physical Review* **124**, 1866 (1961).
- [111] Y. S. Joe, A. M. Satanin, and C. S. Kim, “Classical analogy of fano resonances”, *Physica Scripta* **74**, 259 (2006).
- [112] G. Kim, S. B. Lee, T.-S. Kim, and J. Ihm, “Fano resonance and orbital filtering in multiply connected carbon nanotubes”, *Physical Review B* **71**, 205415 (2005).
- [113] A. Johnson, C. M. Marcus, M. Hanson, and A. Gossard, “Coulomb-modified fano resonance in a one-lead quantum dot”, *Physical Review Letters* **93**, 106803 (2004).
- [114] F. Hao, Y. Sonnefraud, P. V. Dorpe, S. A. Maier, N. J. Halas, and P. Nordlander, “Symmetry breaking in plasmonic nanocavities: subradiant lspr sensing and a tunable fano resonance”, *Nano letters* **8**, 3983 (2008).
- [115] J. Song, Y. Ochiai, and J. Bird, “Fano resonances in open quantum dots and their application as spin filters”, *Applied physics letters* **82**, 4561 (2003).
- [116] F. Hao, P. Nordlander, Y. Sonnefraud, P. V. Dorpe, and S. A. Maier, “Tunability of subradiant dipolar and fano-type plasmon resonances in metallic ring/disk cavities: implications for nanoscale optical sensing”, *ACS nano* **3**, 643 (2009).
- [117] N. Liu, T. Weiss, M. Mesch, L. Langguth, U. Eigenthaler, M. Hirscher, C. Sonnichsen, and H. Giessen, “Planar metamaterial analogue of electromagnetically induced transparency for plasmonic sensing”, *Nano letters* **10**, 1103 (2009).

- [118] A. E. Nikolaenko, F. De Angelis, S. A. Boden, N. Papasimakis, P. Ashburn, E. Di Fabrizio, and N. I. Zheludev, “Carbon nanotubes in a photonic metamaterial”, *Physical Review Letters* **104**, 153902 (2010).
- [119] P. A. Kuchment, *Floquet theory for partial differential equations*, Vol. 60 (Birkhäuser, 2012).
- [120] G. Floquet, “Sur les équations différentielles linéaires à coefficients périodiques”, in *Annales scientifiques de l’école normale supérieure*, Vol. 12 (1883), pp. 47–88.
- [121] A. Lopez, Z. Sun, and J. Schliemann, “Floquet spin states in graphene under ac-driven spin-orbit interaction”, *Physical Review B* **85**, 205428 (2012).
- [122] G. Goldstein, C. Aron, and C. Chamon, “Photoinduced superconductivity in semiconductors”, *Physical Review B* **91**, 054517 (2015).
- [123] A. Zenesini, H. Lignier, D. Ciampini, O. Morsch, and E. Arimondo, “Coherent control of dressed matter waves”, *Physical Review Letters* **102**, 100403 (2009).
- [124] A. Cottey, “Floquet’s theorem and band theory in one dimension”, *American Journal of Physics* **39**, 1235 (1971).
- [125] A. Eckardt and E. Anisimovas, “High-frequency approximation for periodically driven quantum systems from a floquet-space perspective”, *New Journal of Physics* **17**, 093039 (2015).
- [126] R. Landauer, “Residual resistivity dipoles”, *Zeitschrift für Physik B Condensed Matter* **21**, 247 (1975).
- [127] M Büttiker, “Scattering theory of thermal and excess noise in open conductors”, *Physical Review Letters* **65**, 2901 (1990).
- [128] S. Datta, *Electronic transport in mesoscopic systems* (Cambridge university press, 1997).
- [129] R. Landauer, “Spatial variation of currents and fields due to localized scatterers in metallic conduction”, *IBM Journal of Research and Development* **1**, 223 (1957).
- [130] B. Van Wees, H Van Houten, C. Beenakker, J. G. Williamson, L. Kouwenhoven, D Van der Marel, and C. Foxon, “Quantized conductance of point contacts in a two-dimensional electron gas”, *Physical Review Letters* **60**, 848 (1988).
- [131] M Büttiker, A Prêtre, and H Thomas, “Dynamic conductance and the scattering matrix of small conductors”, *Physical Review Letters* **70**, 4114 (1993).
- [132] Y. M. Blanter and M. Büttiker, “Shot noise in mesoscopic conductors”, *Physics reports* **336**, 1 (2000).

- [133] L. Arrachea and M. Moskalets, “Relation between scattering-matrix and keldysh formalisms for quantum transport driven by time-periodic fields”, *Physical Review B* **74**, 245322 (2006).
- [134] M. V. Moskalets, *Scattering matrix approach to non-stationary quantum transport* (World Scientific, 2011).
- [135] M. Buttiker, “Capacitance, admittance, and rectification properties of small conductors”, *Journal of Physics: Condensed Matter* **5**, 9361 (1993).
- [136] M Büttiker, “Time-dependent current partition in mesoscopic conductors”, *Il Nuovo Cimento B (1971-1996)* **110**, 509 (1995).
- [137] M. Büttiker, “Time-dependent transport in mesoscopic structures”, *Journal of Low Temperature Physics* **118**, 519 (2000).
- [138] J. Tworzydło, B. Trauzettel, M. Titov, A. Rycerz, and C. W. Beenakker, “Sub-poissonian shot noise in graphene”, *Physical Review Letters* **96**, 246802 (2006).
- [139] Z. Wang, Z. Zhang, H. Xu, L. Ding, S. Wang, and L.-M. Peng, “A high-performance top-gate graphene field-effect transistor based frequency doubler”, *Applied Physics Letters* **96**, 173104 (2010).
- [140] T. Palacios, A. Hsu, and H. Wang, “Applications of graphene devices in rf communications”, *IEEE Communications Magazine* **48** (2010).
- [141] V. N. Kotov, B. Uchoa, V. M. Pereira, F Guinea, and A. C. Neto, “Electron-electron interactions in graphene: current status and perspectives”, *Reviews of Modern Physics* **84**, 1067 (2012).